Geostatistical Analysis and Mitigation of the Atmospheric Phase Screens in Ku-Band Terrestrial Radar Interferometric Observations of an Alpine Glacier

Simone Baffelli, *Student Member, IEEE*, Othmar Frey, *Senior Member, IEEE*, and Irena Hajnsek, *Fellow, IEEE*

Abstract—**Terrestrial radar interferometry (TRI) can measure displacements at high temporal resolution, potentially with high accuracy. An application of this method is the observation of the surface flow velocity of steep, fast-flowing aglaciers. For these observations, the main factor limiting the accuracy of TRI observations is the spatial and temporal variabilities in the distribution of atmospheric water vapor content, causing a phase delay [atmospheric phase screen (APS)] whose magnitude is similar to the displacement phase. This contribution presents a geostatistical analysis of the spatial and temporal behaviors of the APS in Ku-Band TRI. The analysis is based on the assumption of a separable spatiotemporal covariance structure, which is tested empirically using variogram analysis. From this analysis, spatial and temporal APS statistics are estimated and used in a two-step procedure combining regression-Kriging with generalized least squares (GLS) inversion to estimate a velocity time-series. The performance of this method is evaluated by cross-validation using phase observations on stable scatterers. This analysis shows a considerable reduction in residual phase variance compared with the standard approach of combining the linear models of APS stratification and interferogram stacking.**

Index Terms—**Atmospheric modeling, atmospheric phase screen (APS), differential radar interferometry (D-InSAR), synthetic aperture radar (SAR), terrestrial radar interferometry (TRI).**

I. INTRODUCTION

A. Motivation

AVALANCHING glaciers [1], [2] can pose a hazard to Alpine Valleys. Ice calving at their terminus has major consequences, directly, through the subsequent ice avalanche and, indirectly, since the falling ice mass can trigger other phenomena such as floods, snow avalanches, and debris flows,

which have severe consequences. The 1956 disaster at the Mattmark dam construction site [3], the 1962 and 1967 Mount Huascaran avalanches, and the 2002 Kazbek massif debris flow [4] are the examples of the consequences of such collapses [1].

Recent advances in the understanding of glacier failures [1] suggest the possibility of early detection of developing glacier failures. In the case of steep, unbalanced cold glaciers, such as in the Weisshorn hanging glacier [2], [5], [6], mechanical instabilities in the ice are the main mechanisms leading to the break-off events, where the rupture happens within the ice mass. A log-periodic oscillation of the surface velocity superimposed to a power-law acceleration is observed in these cases [6]. This behavior may reveal to be useful to predict the break-off times if frequent observations of the surface velocity are available.

For steep, temperate glaciers, sliding is the main source of instability, leading to break offs. Subglacial water pressure reduces basal friction, causing a major portion of the tongue to become unstable [7] and eventually to break off. An example is the Allalingletscher, responsible for the 1956 Mattmark disaster. In this type of glacier, the surface velocity increases during the *active phases*, notably in summer [1]. Despite this, these patterns only rarely correlate with the break-off events; surface velocity measurements alone are insufficient and should be combined with other methods such as seismic measurements [8].

For both glacier types, reliable and precise measures of surface velocities are necessary for monitoring and improving the understanding of their dynamics. Area-wide estimates at high temporal resolution and over long periods of time are particularly useful.

Remote-sensing techniques [9]–[11] are frequently employed for glacier flow measurements, using visible and infrared images [12]–[14] or coherent [15]–[19] and incoherent [17], [20] methods with spaceborne and terrestrial [21]–[25] synthetic aperture radar (SAR) data.

In this context, terrestrial radar interferometry (TRI) [21]–[25] is complementary to the more established space- and airborne SAR observations. While the spatial coverage of TRI is normally smaller, these systems offer great flexibility

in the acquisition geometry and timing, both of which are necessary to sample the fast dynamics of the avalanching glaciers. Moreover, radar data are independent of external illumination and can acquire data through fog and clouds, permitting continuous observations during night and with cloud cover.

These observations are evaluated using differential radar interferometry (D-InSAR) [26], which uses the sensitivity of the phase of microwaves to the length of the propagation path from the sensor to the observed surface. By computing the difference in the phase measurements at subsequent times, D-InSAR can estimate the displacements with a precision theoretically limited by the wavelength employed by the radar.

Variations in the spatial distribution of the atmospheric water vapor content causing time-varying spatial heterogeneity in the propagation speed of light are one of the largest sources of errors in displacement estimation with differential radar interferometry. These nuisances are known as atmospheric phase screen (APS) [27]–[29].

Precise estimation of displacements with D-InSAR requires phase calibration to remove—or at least mitigate—the phase contribution caused by the APS.

This task has been extensively studied for spaceborne InSAR, but in smaller measure for TRI observations, owing to the scarcity of these data sets. The different acquisition geometries and the short revisit times frequently employed in these cases suggest a reevaluation of current APS correction strategies as these were originally developed for spaceborne InSAR observations.

B. State of the Art

The atmosphere is a complex, dynamic system: temporal fluctuations of temperature, pressure, and water vapor content [30] and their heterogeneous spatial distribution produce spatial and temporal variations in atmospheric refractivity and, thus, of the propagation delay of EM waves, which are observed as APS in differential radar interferometries.

Auxiliary observations are sometimes employed to model the distribution of refractivity at the time of acquisitions and, hence, correct phase delays in interferometric observations. Examples of these observations are weather model outputs [31], wet zenith delay (WZD) maps derived from global navigation satellite system (GNSS) observations [27], [32]–[34], or maps of water vapor distributions obtained from spaceborne microwave radiometers and imaging spectrometers [35]–[38].

In most cases, APS-estimation methods are based on the composite model of atmospheric phase delay partitioning its variability [39], [40] between a deterministic and a stochastic contribution.

The first component is a phase screen of low spatial frequency, attributed to vertical stratification [31], [41]–[48], often observed to correlate with topography.

The stochastic contribution is associated with turbulent mixing of water vapor in the troposphere. This component is highly variable in space and time and cannot be modeled with the deterministic approaches. Because it is correlated

with space, it is described using the spatial covariance or semivariance functions [29], [30], [32] that can be derived from the turbulence theory [30], [49].

The turbulent contribution is frequently assumed to be uncorrelated with time [39], [50], [51]. Thanks to this assumption, the APS is separated from other phase nuisances and the deformation phase using time-series analysis applied on a set of scatterers whose phase is stable with time and *persistent scatterers* (PSs) [52]. This gives a pointwise estimate of the APS, which is extrapolated to a grid, covering the area of interest using geostatistical interpolators that consider the spatially correlated nature of the observations such as Kriging [50], [53].

The extrapolated APS is subtracted from the interferometric phase observations, which are then processed to estimate the displacement signal [54], [55].

C. Research Gaps

Solutions based on external data are mainly applicable to spaceborne InSAR, since, in terrestrial observations, the size of the scene is much smaller than the resolutions of these auxiliary observations and of the extent of the deformation to monitor.

Moreover, in TRI, only a portion of the atmospheric air column is traversed, while the auxiliary data acquired from space would give the total phase delay through the entire height of the troposphere.

These limitations nontwithstanding, similar concepts employing automatic weather station (AWS) data exist for TRI [44], [56]. Unfortunately, such measurements are often not available during a TRI monitoring campaign. Even if they were, these approaches can only correct large-scale, low-frequency phase variations and cannot compensate local high spatial-frequency phase variations.

These limitations motivate the development of the APS correction approaches based only on the statistical behavior of the APS, which do not rely on the auxiliary measurements.

The applicability of the statistical assumptions used in spaceborne D-InSAR to TRI is doubtful because of the smaller spatial coverage of the data and the different acquisition geometry.

In the TRI case, the radar signal propagates through a small vertical portion of the troposphere, while, in spaceborne SAR, the entire height of the atmosphere is traversed. These differences mean that both the deterministic models of the stratified APS and the statistical model of turbulence derived for the spaceborne InSAR may not apply to TRI observations.

The smaller the scene size, the shorter the vertical propagation path, and—in the case of observation of fast displacements—the short time interval between the acquisitions in TRI reduces the magnitude of atmospheric stratification, negatively affecting the performance of the APS stratification models in the TRI case.

With respect to the turbulent APS, the statistical assumption of temporal uncorrelatedness must be evaluated considering the shorter revisit times often used in TRI. In this context, using parameter estimators accounting for correlation leads to

This article has been accepted for inclusion in a future issue of this journal. Content is final as presented, with the exception of pagination.

BAFFELLI *et al.*: GEOSTATISTICAL ANALYSIS AND MITIGATION OF THE APSs

3

more efficient estimators and to more robust inference of the parameter estimate uncertainity.

D. Contributions of This Article

This article presents a geostatistical analysis of the APS [27]–[29], affecting the Ku-band TRI data with the aim to bridge the above research gaps.

To do so, the study starts from the APS model customarily employed in the In-SAR studies, assuming a combination of the turbulent and stratified atmosphere. From this mathematical foundation, a number of issues are investigated.

1) The performance of several models of APS stratification is quantified by measuring their ability to describe the phase variance observed at a set of PSs. These points are chosen at the locations known to be affected by atmospheric disturbances only.
2) The assumption of spatially correlated, temporally uncorrelated APS statistics—common for spaceborne InSAR data—is replaced by a separable spatiotemporal covariance model. The suitability of this model is tested by variogram analysis.
3) The performance of APS correction using a regression-Kriging interpolator accounting for stratification effects and a spatial covariance model of turbulence is evaluated. Its performance is evaluated by computing the residual phase variance at a set of nonmoving PS.
4) A time-series inversion approach employing the temporal covariance model is presented. Its performance in mitigating the residual APS observed after regression-Kriging correction is assessed.

II. METHODS

A. Differential Radar Interferometry: Signal Model

Differential radar interferometry [57], [58] uses the phase coherence of radar images to measure the displacements. This is possible because each scatterer phase as measured by such a radar contains a contribution proportional to the line-of-sight (LOS) distance from the sensor to the object.

Consequently, the phase difference between a pair of images taken at different times contains a term proportional to the displacement of the scatterers composing the scene.

More formally, start by considering a radar placed at the origin $\mathbf{0}$ of a Cartesian coordinate system. In the same frame, consider a scatterer located at $\mathbf{s}$ at time t_k. Its phase as measured by the radar is

$$\phi(t_k) = \frac{4\pi}{\lambda} R(t_k) + \phi_{\text{scat}}(t_k) + \phi_{\text{atm}}(t_k) \tag{1}$$

where $R = |\mathbf{s}|$ is the distance between the scatterer and the sensor and ϕ_{scat} is the scattering phase, which depends on the object's dielectric properties, shape, and a radar-specific phase offset due to the delays in the device's circuits. λ is the wavelength and ϕ_{atm} is the excess phase delay caused by refraction in the atmosphere.

At a scatterer moving with velocity $v = (\Delta R/t_{l+m} - t_l)$ along the LOS in a period of duration Δt between times t_l

and t_{l+m}, the *interferometric phase* or *interferometric phase difference* is

$$\Delta\phi = \frac{4\pi}{\lambda} \Delta R + 2\pi n + \epsilon_{\text{atm}} + \epsilon_{\text{decorr}}$$

$$= \frac{4\pi}{\lambda} \Delta t v + 2\pi n + \epsilon_{\text{atm}} + \epsilon_{\text{decorr}} \tag{2}$$

where Δ_t is the *temporal baseline*, the term $2\pi n$ indicates that phase measurements are the ambiguous modulo half the wavelength, $(\lambda/2)$, $\epsilon_{\text{atm}} = \phi_{\text{atm}}(t_{l+m}) - \phi_{\text{atm}}(t_l)$ represents the additional *differential* phase delay due to changes in atmospheric refractivity, ϵ_{decorr} describes the noise-like phase error due to thermal noise in the radar, and ϕ_{scat} models the phase error due to variations in the scatterer's properties.

Equation (2) shows that the interferometric phase difference is sensitive to the displacement ΔR but also to the changes in the dielectric properties of the imaged objects and to the changes in the propagation medium.

In differential interferometry, the objective is the estimation of the displacement ΔR—or the velocity v—from these noisy phase observations. Consequently, all terms and the displacement are considered nuisances.

To improve the displacement-estimation robustness—and possibly to estimate an object's displacement history—multiple phase measurements at different times are often used. Thus, the model describing a single interferometric phase observation of (2) is extended to multiple observations as follows.

Given a vector $\mathbf{y}$ of PN radar phases $y(i, l)$ derived from single look complex (SLC) data acquired at N times t_k and P locations $\mathbf{s}_i$, estimate the (PN)-element vector $\mathbf{v}$ of surface velocities $v(i, l)$ at times $t_l = (t_k + t_{k+1}/2)$ with $0 < k < N$ between subsequent acquisitions at locations $\mathbf{s}_i$ with $0 < i < P$ [59], [60].

In analogy with (2), it is convenient to replace the SLC phase vector $\mathbf{y}$ with the PM-dimensional vector of the interferometric phases $\mathbf{z}$

$$\mathbf{z} = \bar{\mathbf{A}}\mathbf{y} \tag{3}$$

where $\mathbf{z}$ is a PM-dimensional vector of phase differences at P locations and M times.

Here, M is the number of interferograms, with $N < \frac{N+1}{2}$, the number of unique pairs that can be formed from N SLC images.

The matrix $\bar{\mathbf{A}} = \mathbf{I}_P \otimes \mathbf{A}$ is the incidence matrix; an $MP \times NP$ is the block-diagonal matrix used to compute the interferometric phases from the SLC phase vector. Each of its blocks $\mathbf{A}$ indicates which of the N acquisitions are paired to form interferograms in $\mathbf{z}$: entries A_{mk} and A_{ml} are -1 and 1 for the mth interferogram between the lth and the kth acquisition. As an example, given four SLC images, the matrix $\mathbf{A}$ that gives the three unique interferometric pairs between subsequent acquisitions is

$$A = \begin{bmatrix} 1 & -1 & 0 & 0 \\ 0 & 1 & -1 & 0 \\ 0 & 0 & 1 & -1 \end{bmatrix}. \tag{4}$$

The (PN)-element vector of velocities $\mathbf{v}$ can be related to the vector of interferometric phases [30], [39], [59], [60] in

analogy with (2)

$$\mathbf{z} = \bar{\mathbf{B}}\mathbf{v} + \epsilon_z \qquad (5)$$

where $\bar{\mathbf{B}} = \mathbf{I}_P \otimes \mathbf{B}$ and $\mathbf{B}$ is an $M \times N$ matrix of the time spans between the acquisition times of the SLC images. Its construction from the interferogram incidence matrix $\mathbf{A}$ has been described elsewhere [59]. As an example, using the incidence matrix $\mathbf{A}$ of (4) and assuming regularly spaced acquisitions with Δt temporal separation, $\mathbf{B}$ will be

$$\mathbf{B} = \begin{bmatrix} \Delta t & 0 & 0 & 0 \\ 0 & \Delta t & 0 & 0 \\ 0 & 0 & \Delta t & 0 \end{bmatrix}. \qquad (6)$$

Finally, ϵ_z is a term subsuming all the noise-like contributions, assumed to be a zero-mean Gaussian random process with a $PM \times PM$ covariance matrix Σ_z, describing the spatial and temporal correlations of the nuisance terms.

As the phase nuisance is assumed to be drawn from a multivariate Gaussian distribution of known covariance, the generalized least squares (GLS) solution of (5) is the minimum variance, unbiased estimator for $\mathbf{v}$ [61], [62]

$$\hat{\mathbf{v}} = (\bar{\mathbf{B}}^T \Sigma_z^{-1} \bar{\mathbf{B}}) \bar{\mathbf{B}}^T \Sigma_z^{-1} \mathbf{z}. \qquad (7)$$

In many cases, acquisitions too distant in time cannot be used to form interferograms, because they would show a high level of phase noise caused by temporal decorrelation and will be affected by phase wrapping. Therefore, $\mathbf{A}$ will consists of only those rows where the temporal baseline is shorter than a given threshold; thus, $M < ((N)(N-1)/2)$ and the rank of $\mathbf{B}$ is deficient. In that case, the problem is underdetermined and there is no unique solution for $\mathbf{v}$. An example of this situation is shown in (6), where only three interferograms are available to estimate four parameters.

Decorrelation is mitigated by the PS approaches, where only observations at highly coherent scatterers [50], [52], [63] unaffected by temporal decorrelation are used for inversion. This approach permits to increase the system's rank by using interferometric pairs that would have been discarded because of phase decorrelation when evaluated with conventional interferometric techniques.

In practice, these methods are of little use in the case reported in this paper, since the constantly changing surface features and the rapid motion of glaciers make the detection of PS very unlikely.

As an alternative, the rank of (5) can be increased by using a simplified velocity model, described by a vector $\mathbf{p}$ with a smaller number of parameters $d < PN$ [59]

$$\mathbf{v} = \mathbf{M}\mathbf{p}. \qquad (8)$$

Assuming constant velocity v_0 over time, the model for the ith pixel is

$$\mathbf{v}_i = \begin{bmatrix} v_0 \\ \vdots \\ v_0 \end{bmatrix} = \mathbf{I}_{N,1} v_0 = \mathbf{M}_i \mathbf{p} \qquad (9)$$

and $\mathbf{M}$ is the block-diagonal matrix $\mathbf{I}_{N,1} \otimes \mathbf{I}_{N,P}$.

$\mathbf{M}$ can be any $PN \times d$ matrix describing a simplified spatial and temporal displacement model and possibly enforcing the spatiotemporal smoothness constraints.

The constrained problem is rewritten as

$$\mathbf{z} = \bar{\mathbf{B}}\mathbf{M}\mathbf{p} + \epsilon_z = \bar{\mathbf{G}}\mathbf{p} + \epsilon_z \qquad (10)$$

where the *design matrix* $\bar{\mathbf{G}}$ is written with a bar to indicate that it is the design matrix for the whole set of P pixels in the set of all M interferograms. For simplicity, $\bar{\mathbf{G}}$ is assumed to be a block matrix with P blocks $\mathbf{G}$—the same velocity model is assumed for each pixel and no spatial constraints are set.

The GLS estimate of $\mathbf{p}$ is obtained with

$$\hat{\mathbf{p}} = (\bar{\mathbf{G}}^T \Sigma_z^{-1} \bar{\mathbf{G}}) \bar{\mathbf{G}}^T \Sigma_z^{-1} \mathbf{z}. \qquad (11)$$

The variance of the estimates is

$$\mathrm{var}(\hat{\mathbf{p}}) = \bar{\mathbf{G}}^T \Sigma_z^{-1} \bar{\mathbf{G}}. \qquad (12)$$

Without further assumptions, the only constraint for the covariance matrix of the nuisance Σ_z is that it must be positive-semidefinite. As the APS is known to be spatially correlated and potentially correlated with time, its inversion for (11) may be computationally costly [39] because of its large size.

By making certain assumptions to be discussed later, the spatially correlated contributions in Σ_z can be estimated and removed before the least-squares inversion. By doing so, a new data set is obtained, where the APS is approximately uncorrelated with space, making the inversion computationally easier.

Whether the full inversion is attempted or the latter approach is used, knowledge of the covariance matrix of the interferogram network is required for the inversion and to provide uncertainty estimates or to make reliable inferences about the derived parameters.

As the interferometric phases $\mathbf{z}$ are derived from the SLC phases by (3), the interferogram covariance is related to the covariance of the SLC phase vector $\mathbf{y}$ [39]

$$\Sigma_z = \bar{\mathbf{A}}\Sigma_y\bar{\mathbf{A}}^T. \qquad (13)$$

ϵ_y is [30], [39]

$$\epsilon_y = \epsilon_{y,\mathrm{atm}} + \epsilon_{y,\mathrm{decorr}} \qquad (14)$$

where $\epsilon_{y,\mathrm{atm}}$ is the phase contribution from the APS and $\epsilon_{y,\mathrm{decorr}}$ represents the phase noise due to temporal decorrelation in each acquisition. These two terms are mutually uncorrelated, because they are produced by different physical mechanisms and are expressed as a sum of independent covariance matrices.

When referencing to the SLC phase, the noise terms must be seen as deviations from the noise-free SLC phases consisting only of the propagation term and the intrinsic scattering phase as in (1) [39]. These equations are only a tool to model the covariance of the interferometric phases, because the true SLC phases themselves cannot be observed directly: the effect of the nuisances and of displacement is only visible in the differential phases that are computed using (3).

With (3), the covariance matrix of the interferometric phase vector Σ_z is obtained as

$$\Sigma_z = \Sigma_{z,\mathrm{atm}} + \Sigma_{z,\mathrm{decorr}}. \qquad (15)$$

The following sections are dedicated to the individual covariance terms.

1) Covariance of Decorrelation Phase Noise: $\Sigma_{z,\text{decorr}}$ models the effect of thermal noise in the measurement system and random changes in reflectivity on the stability of the observed interferometric phases. This is usually quantified through the magnitude of the interferometric phase coherence, γ [64], derived from spatial or temporal multilooking by assuming ergodicity [65]. The coherence magnitude is used to estimate the interferometric phase variance through the Cramer–Rao lower bound [66].

The phase variance for an interferogram pixel located at $\mathbf{s}_i$ at time $t_l = (t_o + t_p/2)$, derived from acquisitions at times t_o and t_p, is

$$\text{Var}[z_{i,o,p}] \geq \frac{\sqrt{1 - \gamma_{i,o,p}^2}}{\gamma_{i,o,p}\sqrt{2L}} \qquad (16)$$

where the notation $\gamma_{i,o,p}$ indicates the coherence estimate at pixel i from acquisitions o and p.

In the case considered here, with interferograms acquired at zero spatial baseline, the decorrelation noise is spatially uncorrelated. $\Sigma_{z,\text{decorr}}$ is a block-diagonal matrix, where each $M \times M$ block represents the covariance of the decorrelation process for an individual pixel [39].

In this article, the temporal covariance $\Sigma_{z,\text{decorr}}(i)$ for the ith pixel is assumed to follow the Brownian decorrelation model. This is derived assuming that the incremental displacement of each scatterer composing a resolution cell is drawn from a uniform distribution [39], [64], [67]. This gives an exponential decay in the coherence as a function of the time between acquisitions

$$\gamma(\Delta T) = \gamma_0 e^{\frac{-\Delta t}{\tau}}. \qquad (17)$$

The Brownian model is not suitable for all terrain types; it was found to be applicable to urban areas in [67]. In many cases, the coherence shows complex patterns as seasonal trends or variations correlated with weather conditions. These situations are not modeled in this article.

2) Covariance of APS : The term $\epsilon_{y,\text{atm}}$ models the phase delay caused by the inhomogeneous distribution of atmospheric water vapor in the scene [27]–[29]. Its effect cannot be appreciated in the SLC phase and only in interferograms: temporal changes in the spatial distribution of atmospheric delay $\epsilon_{y,\text{atm}}$ between the acquisitions appear in the interferometric phase difference as low spatial-frequency phase screens that mask the displacement phase.

Part of these phase trends are reasonably approximated—at least for spaceborne D-InSAR—by the linear models assuming homogeneous or layered distributions of atmospheric water vapor [31], [41]–[48]. These models are often not sufficient to capture the full APS phase variability and must be augmented with a statistical description.

Therefore, the APS is written as the superposition of these terms [39], [40]

$$\epsilon_{y,\text{atm}} = \epsilon_{y,\text{atm,strat}} + \epsilon_{y,\text{atm,turb}} \qquad (18)$$

where $\epsilon_{y,\text{atm,strat}}$ is the *stratified* APS and $\epsilon_{y,\text{atm,turb}}$ is the *turbulent* APS, due to turbulent mixing in the troposphere [30], [32], which is modeled statistically as a zero-mean second-order stationary Gaussian random process with covariance matrix $\Sigma_{y,\text{atm}}$.

More precisely, the random process generating the APS can be described through a covariance matrix $\Sigma_{y,\text{atm}}$ if and only if its covariance function C is *stationary* in space and time. This means that C depends only on the spatial separation $\mathbf{d} = \mathbf{s_1} - \mathbf{s_2}$ and on the temporal lag $t = t_1 - t_2$, and not on the locations themselves [68]. This assumption is frequently combined by the assumption of *isotropy* in space, where C depends only on the length $d = |\mathbf{d}|$ and not on the vector's direction.

In the spaceborne InSAR studies, the APS covariance is further simplified by assuming lack of temporal correlation [39]; thus

$$C(d, t) = C_s(d)\,\delta(t) \qquad (19)$$

where $\delta(t)$ is the Dirac delta distribution. The assumption of uncorrelatedness with time is justified in the spaceborne InSAR, because the acquisition repetition times are in the order of days, where it is expected that the turbulent behavior in the troposphere changes completely.

This assumption is a special case of the more general property of *separability*, which is assumed in this article. A *separable* covariance function C can be factorized in the product of temporal and spatial covariances

$$C(d, t) = C_t(t)\,C_s(d). \qquad (20)$$

Separability implies that the spatial statistics are not a function of time, a very strict assumption. As an example, it is violated by *Taylor's hypothesis* [28], [29], [33], [34], [68]–[70]. In the latter, it is assumed that turbulent eddies are transported by a wind field $\mathbf{v}$ that does not change their structure.

Therefore, the temporal covariance function can be written as a function of the spatial covariance and of the velocity field $\mathbf{v}$

$$C_t(\mathbf{d}, t) = C_s(\mathbf{d} - \mathbf{v}t). \qquad (21)$$

Despite its limitations, separability is very useful in practice, as it simplifies fitting the statistical models and substantially reduces the size of the covariance matrices.

Consider the APS covariance matrix of the SLC phase vector—the discrete form of the covariance function in (20). In the stationary and separable cases, this matrix can be written as a Kronecker product of a $P \times P$ spatial covariance matrix $\Sigma_{y,\text{atm},s}$ and of an $N \times N$ temporal covariance matrix $\Sigma_{y,\text{atm},t}$ [39], [71]

$$\Sigma_{y,\text{atm}} = \Sigma_{y,\text{atm},s} \otimes \Sigma_{y,\text{atm},t}. \qquad (22)$$

Using (13), the APS covariance matrix of the interferogram vector is

$$\begin{aligned}
\Sigma_{z,\text{atm}} &= \bar{\mathbf{A}}\Sigma_{y,\text{atm}}\bar{\mathbf{A}}^T \\
&= (\mathbf{I} \otimes \mathbf{A})(\Sigma_{y,\text{atm},s} \otimes \Sigma_{y,\text{atm},t})(\mathbf{A}^T \otimes \mathbf{I}^T) \\
&= \Sigma_{y,\text{atm},s} \otimes (\mathbf{A}\Sigma_{y,\text{atm},t}\mathbf{A}^T)
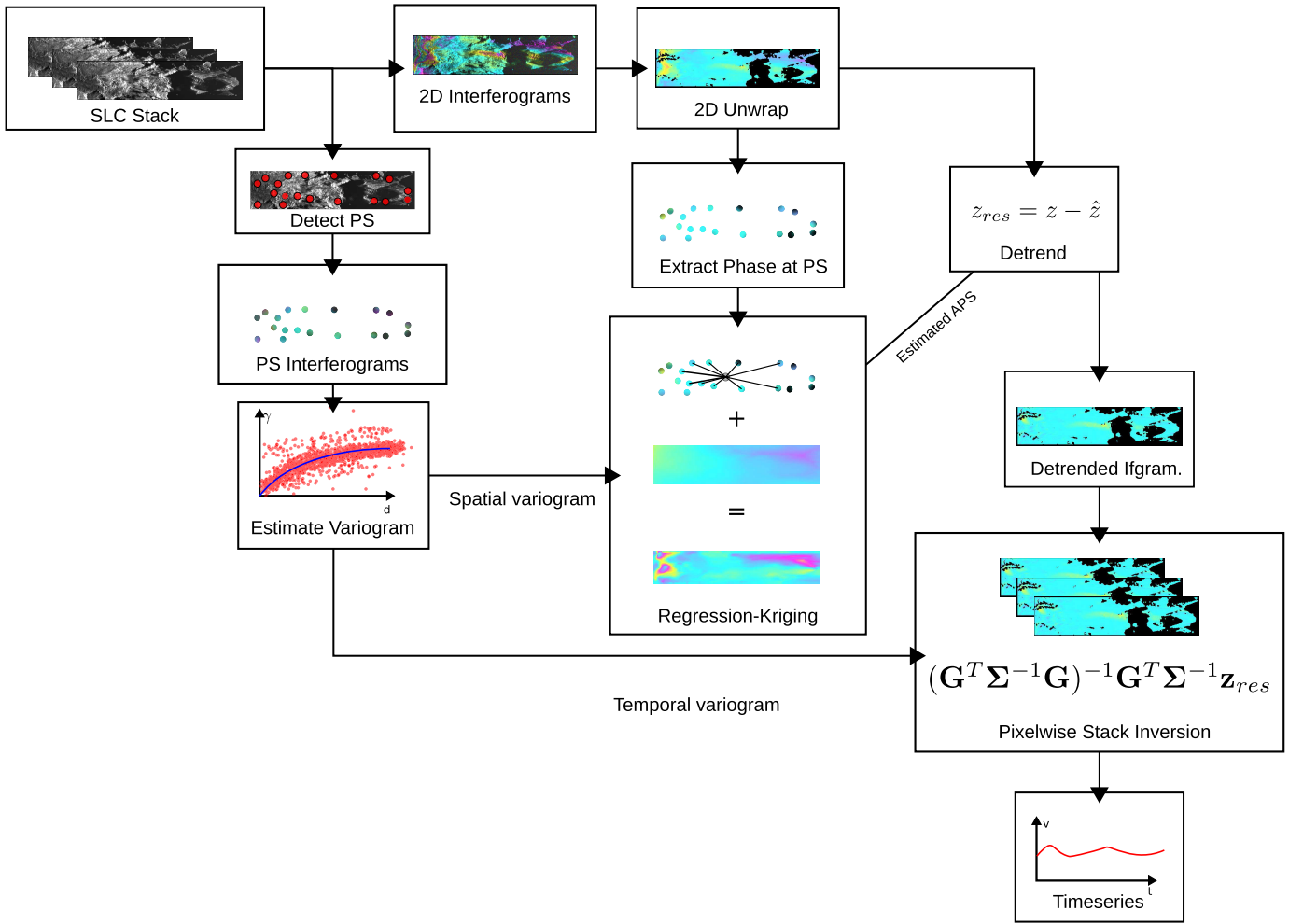\end{aligned} \qquad (23)$$

Fig. 1.   Schematic of the two-step spatial APS mitigation and time-series inversion.

where the last step follows from the mixed-product property of the Kronecker product.

In summary, the considerations made above, combined with spatiotemporal separability, lead to the following APS model.

1) Assuming the APS in the SLC phase vector to have a separable covariance, the APS in the interferogram vector has separable covariance as well. The estimation and correction of the spatially and temporally correlated components can be performed separately.

2) The turbulent APS contribution in the interferogram phase vector has the same spatial covariance matrix as the *unobservable* APS in the SLC phase vector. This covariance does not vary over time.

3) If a linear model is used to describe the stratified APS in the SLC phase, the stratified APS observed in an interferogram is described by a model with the same functional form.

3) Inversion Strategy: In summary, ϵ_z, the noise affecting the interferograms is assumed to be a zero-mean Gaussian random vector with covariance

$$\Sigma_z = \Sigma_{y,\text{atm},s} \otimes (\mathbf{A}\Sigma_{y,\text{atm},t}\mathbf{A}^T) + \Sigma_{z,\text{decorr}} \qquad (24)$$

where $\Sigma_{y,\text{atm},s}$ is the $P \times P$ matrix of the spatial APS covariance, $\Sigma_{y,\text{atm},t}$ the $N \times N$ matrix of the temporal APS covariance, and $\Sigma_{z,\text{decorr}}$ is the $PM \times PM$ diagonal or block-diagonal matrix of the decorrelation phase noise. Finally, each interferogram is affected by a stratified APS, which is assumed to be deterministic and is predicted by a linear model of stratification.

The following procedure is used to estimate the APS affecting the interferogram vector and reconstruct **p**.

1) For each interferogram l at time t_l, an estimate $\hat{\epsilon}_{z,\text{atm}}(t_l)$ of the spatially correlated APS is obtained by regression-Kriging interpolation of the interferometric phases observed on a set of PSs whose phase is unaffected by displacement. These estimates are subtracted from the interferogram vector **z**, reducing the spatial correlation in the residual interferogram vector $\mathbf{z}_{\text{res}}$ to an extent where it is almost negligible.

2) The generalized least squared inversion for **p** can then be applied pixel by pixel on the residual interferogram vector $\mathbf{z}_{\text{res}}$, provided that the design matrix $\bar{\mathbf{G}}$ can be written as a block-diagonal matrix with P blocks and assuming each pixel i to be affected by a spatially uncorrelated, temporally correlated APS and decorrelation

This article has been accepted for inclusion in a future issue of this journal. Content is final as presented, with the exception of pagination.

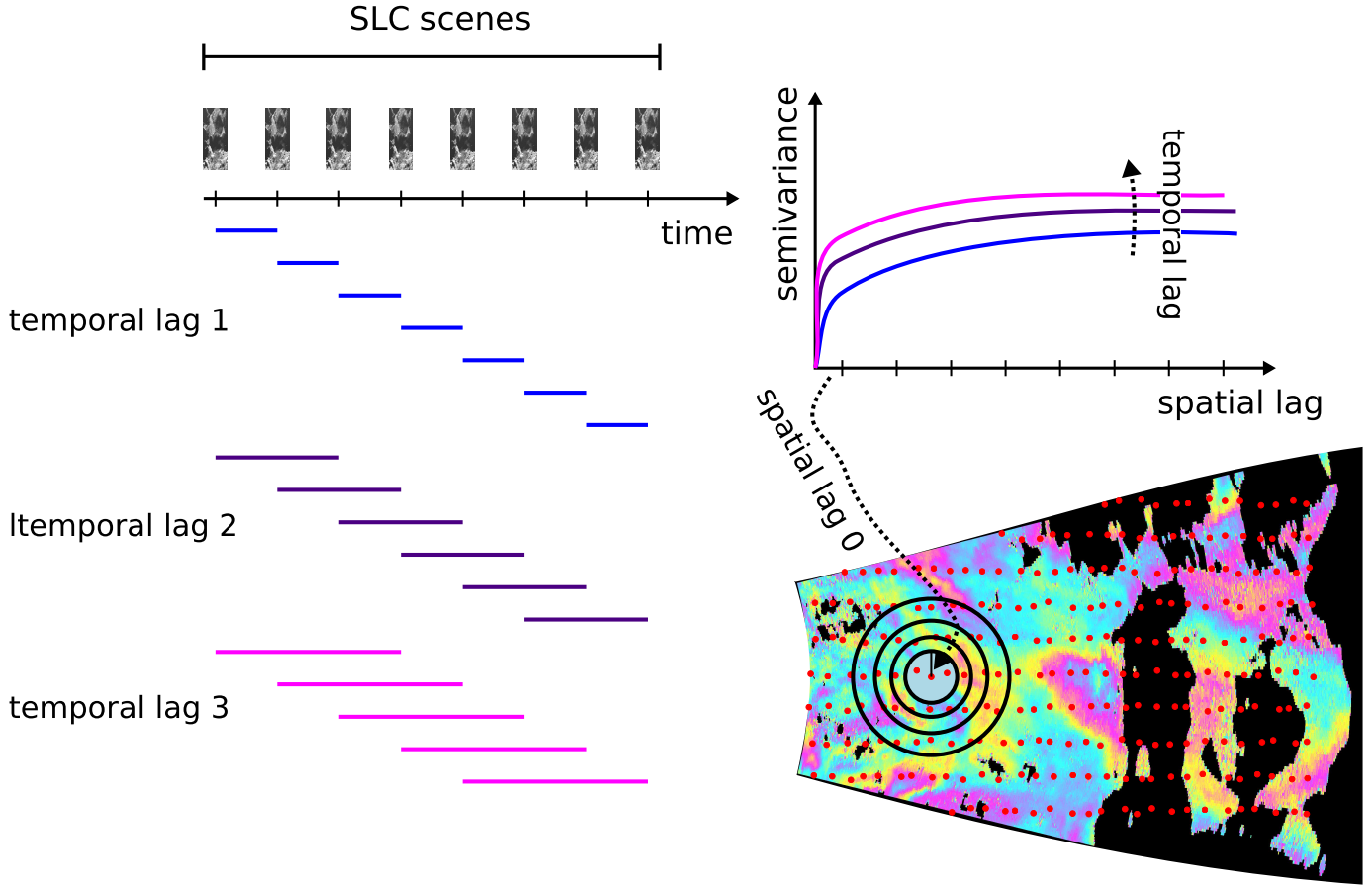BAFFELLI *et al.*: GEOSTATISTICAL ANALYSIS AND MITIGATION OF THE APSs 7

Fig. 2. Illustration of the computation procedure for the spatiotemporal variogram, used to estimate the space–time covariance of the APS, $\Sigma_{y,\text{atm}}$. Assuming separability, the spatial covariance of the APS has the same structure as the covariance of the interferograms and can be estimated as the spatial variogram averaged over all temporal baselines. The temporal variogram corresponds to the mean phase variance of the interferogram grouped by temporal lags.

noise contribution, which is assumed to have a covariance matrix

$$\Sigma_{z,\text{res}}(i) = \Sigma_{z,t}(i)$$
$$= \mathbf{I} \otimes (\mathbf{A}\Sigma_{y,\text{atm},t}\mathbf{A}^T) + \Sigma_{z,\text{decorr}}(i). \quad (25)$$

The correction of the spatially correlated contribution $\epsilon_{y,\text{atm},s}$ will be described in detail in Section II-B, while the pixelwise GLS inversion to obtain the estimates of the displacement parameters is discussed in Section II-C.

A block diagram showing the general principle of the employed APS correction and inversion scheme is shown in Fig. 1. The next sections will be devoted to the discussion of the various steps used in this approach.

B. Spatial Correction of APS

1) Regression-Kriging: According to the model setup, the interferometric phase $z(i,l)$ at time t_l and at any location $\mathbf{s}_i$ is written as the superposition of the displacement phase and the stratified and turbulent APS

$$z(i,l) = z_{\text{disp}}(i,l) + \epsilon_{z,\text{atm}}(i,l)$$
$$= z_{\text{disp}}(i,l) + \epsilon_{z,\text{atm},\text{strat}}(i,l) + \epsilon_{z,\text{atm},\text{turb}}(i,l)$$
$$= z_{\text{disp}}(i,l) + \mathbf{X}\beta(l) + \epsilon_{z,\text{atm},\text{turb}}(i,l) \quad (26)$$

where $\mathbf{X}$ is a matrix of regressors, which are either functions of the coordinates $\mathbf{s}_i$ or auxiliary measurement at these locations.

$\beta(l)$ is the vector of parameters for the stratification model at time t_l and $\epsilon_{z,\text{atm},\text{turb}}$ is the turbulent APS.

To estimate $\hat{\beta}$, a subset S of PSs from the P pixels in the interferogram is used; it is assumed that their phases at any time only consist of the stratified and turbulent APS contributions, with spatial covariance $\Sigma_{z,\text{atm},s}^{\text{PS}}$. The best linear unbiased estimator of $\beta(l)$ is given by the GLS estimator [72]–[74]

$$\hat{\beta}(l) = \left(\mathbf{X}\Sigma_{z,\text{atm},s}^{\text{PS}}{}^{-1}\mathbf{X}\right)^{-1}\Sigma_{z,\text{atm},s}^{\text{PS}}{}^{-1}\mathbf{X}\mathbf{z}(j,l) \quad (27)$$

where $\mathbf{X}$ is the matrix of regressors at locations $\mathbf{s}_j j \in \mathbf{S}$, $\mathbf{z}(j,l)$ the vector of the PS phases, and $\Sigma_{z,\text{atm},s}^{\text{PS}}$ is the spatial covariance of the APS evaluated between the PSs. Using $\hat{\beta}$, the stratified APS contribution at any pixel i in the interferogram can be predicted

$$\hat{\epsilon}_{z,\text{atm},\text{strat}}(i,l) = \mathbf{X}(i,l)\hat{\beta}(l). \quad (28)$$

The solution of (28) does not predict the turbulent component of the APS, which is often the dominant source of phase variability in the interferograms.

Due to the spatial correlation of the APS, it is reasonable to assume that the turbulent APS at a location $\mathbf{s}_i$ near a PS observation $\mathbf{s}_j$, $j \in \mathbf{S}$ is similar to the phase residual—measured phase minus GLS prediction of stratification—of (27) at that PS

$$\epsilon_{\text{res}}^{\text{PS}}(j,l) = z(j,l) - \mathbf{X}(j,l)\hat{\beta}(l). \quad (29)$$

The similarity should decrease with the increasing distance from the PS as the spatial correlation decreases with spatial separation.

At time l, the turbulent APS at $\mathbf{s}_i$ can be approximated as a weighted average of the GLS residuals $\epsilon_{\text{res}}^{\text{PS}}$ at the available PS $\mathbf{s}_j$, $j \in \mathbf{S}$

$$\hat{\epsilon}_{z,\text{atm, turb}}(i,l) = \mathbf{w}(l)\,\epsilon_{\text{res}}^{\text{PS}}(l) \tag{30}$$

where $\mathbf{w}$ is a weight vector, which is a function of the distances between $\mathbf{s}_i$ and $\mathbf{s}_j$, $j \in \mathbf{S}$. Under these conditions, the minimum variance, unbiased estimator for the turbulent APS is given by the Kriging equation [53], [72]

$$\hat{\epsilon}_{z,\text{atm, turb}}(i,l) = \mathbf{v}^T \Sigma_{\text{res}}^{\text{PS}\,-1} \epsilon_{\text{res}}^{\text{PS}} \tag{31}$$

where $\mathbf{v}$ is the vector of spatial APS covariances between $z(i,l)$ and $z(j,l)$, $j \in \mathbf{S}$ and $\Sigma_{\text{res}}^{\text{PS}}$ is the covariance matrix of the regression residuals at the PS.

The predictor of the combined deterministic and turbulent APS at any point $\mathbf{s}_i$ is then the *regression Kriging* estimator

$$\hat{\epsilon}_{z,\text{atm},s}(i,l) = \mathbf{x}(i,l)\,\hat{\beta}(l) + \mathbf{v}^T \Sigma_{\text{res}}^{\text{PS}\,-1} \epsilon_{\text{res}}^{\text{PS}}. \tag{32}$$

A similar approach is presented in [75], where the intrinsic random functions of order k (IRF-k) [76] are used to predict the spatially correlated APS contribution from observations at a set of PS locations. This method is similar to regression Kriging [77], [78], with the difference that, in the form presented in [75], external regressors cannot be employed [78].

In practice, only the nearest K PSs to any prediction point $\mathbf{s}_i$ are used in order to speed up the inversion of $\Sigma_{\text{res}}^{\text{PS}\,-1}$. This is justifiable, since the farther an observation is located to a reconstruction point, the smaller its weight will be.

Furthermore, when the APS is extrapolated to the entire interferogram, the Kriging prediction is computed on a grid whose spacing is larger than the interferogram pixel spacing, and the gaps are filled using a distance-weighted bilinear interpolator.

2) Selection of Stratified APS Model: The choice of a model for the stratified APS component according to (28) needs separate consideration.

Homogeneity and isotropy of the atmospheric refraction index distribution are commonly assumed in the case of terrestrial interferometry, where the scene is often of limited size [41]. These assumptions predict an APS proportional to the range distance from the radar [24], [41]–[43], [47]. To account for spatial inhomogeneities, polynomial models of higher order are proposed [42].

In scenarios with large variations of terrain height, the assumption of homogeneous atmospheric refraction does not apply; a height-dependent term is added as a regressor in the model [45]–[47] to describe the reduction in the atmospheric density with increasing elevation, the *hydrostatic delay*.

Weather parameters [44], [56] can be used to model the variations of the atmospheric refraction index. Since the available weather data are spatially coarse and are of low temporal resolution, this approach is not considered here.

The model commonly employed in TRI processing is summarized in Table I. Here, r represents the slant range from the radar, and h and θ are the elevation and the azimuth angle, respectively. The selection of a stratified APS model best fitting the measurement data is made automatically: the interferometric phases at the PS for a large set of interferograms are used to compute the ordinary least squares (OLS) fit for each model. The fitting is repeated for each of the available interferograms.

The relative performance of the models is evaluated comparing the distribution of the Akaike information criterion (AIC) [80] and of R^2 for the models over the set of interferograms.

The model parameters and the statistics used in model comparison are obtained with OLS and not with the minimum-variance GLS estimator of (27).

This approximation is acceptable, since the goal is the comparison of model performance and not the evaluation of their absolute performance.

3) Spatial Covariance Model for Turbulent APS: Computing the regression-Kriging prediction according to (32) requires the knowledge of $\mathbf{v}$, which is related to the covariance of the APS between two points in space $\mathbf{s}_i$, $\mathbf{s}_j$. Theoretical considerations from the turbulence theory [30], [33], [34], [49], [70], [81] and data derived from the GNSS or spaceborne SAR observations [29], [32], [49] are often employed to derive the APS spatial structure functions [82]—variograms, correlograms, or periodograms—from which the covariance can be determined or approximated.

Nonetheless, the validity of these covariance models in the TRI case is uncertain, given the small number of studies available, the large variability in the acquisition setups, and scene choice and also due to the fact that the imaging geometry specific to TRI is very different to the one in the spaceborne InSAR studies.

Thanks to the assumption of the spatiotemporal separability and isotropy, the spatial covariance function can be estimated from the data using a variogram estimator

$$\gamma_s(d) = \frac{1}{2|N(d)|M_{\text{PS}}} \sum_{l=0}^{M_{\text{PS}}} \sum_{(i,j)\in N(d)} |z(j,l)\,v - z(i,l)|^2 \tag{33}$$

where the sum index l runs over M_{PS} interferograms at different temporal baselines. For each interferogram, the mean-square phase difference between all PSs with spatial separation d, given by the index set $N(d)$, is computed.

Since z is the interferometric phase difference at a fixed location, the empirical spatial variogram estimator corresponds to the mean-squared *double phase difference*—single difference in time and double difference in space, once with respect to the interferogram's reference point and once between any two PSs—over the set of all interferograms.

To reduce the estimation bias caused by the stratified component of the APS in z [83], the variogram γ_s is estimated using the OLS residuals of the stratified model [72].

From this empirical spatial variogram γ_s, a variogram model is fitted using a nonlinear fit; the variogram model is used to obtain an approximation $\hat{\mathbf{v}}$ of the covariance between the

This article has been accepted for inclusion in a future issue of this journal. Content is final as presented, with the exception of pagination.

BAFFELLI *et al.*: GEOSTATISTICAL ANALYSIS AND MITIGATION OF THE APSs

9

TABLE I
SUMMARY OF STRATIFIED APS MODELS EMPLOYED IN TRI

Name	Trend	Comments	References
Unprocessed	$\phi = \beta_0$	No atmospheric trend is modeled; included for performance comparison.	-
Linear	$\phi = \beta_0 + \beta_1 r$	Assumes homogeneous, isotropic atmospheric refraction index. This model is applicable with little topography and small height extents, where no stratification is expected.	[41]–[43]
Quadratic Range	$\phi = \beta_0 + \beta_1 r + \beta_2 r^2$	Models inhomogeneities of refraction index as a linear trend in range.	[24], [42]
Height dependent I	$\phi = \beta_0 + \beta_1 r + \beta_2 rh$	Assumes a horizontally isotropic and homogeneous troposphere with vertical layers [79], resulting in an exponential dependence of refraction index with height, which is approximated to the first order.	[45], [46]
Height dependent II	$\phi = \beta_0 + \beta_1 r + \beta_2 h^2$	Similar assumptions as *Height Dependent I*, here the horizontal and vertical components of refraction are considered to be separable.	[47]
Quadratic 2D Range	$\phi = \beta_0 + \beta_1 r + \beta_2 \theta + \beta_3 \theta r + \beta_4 r^2 + \beta_5 \theta^2$	Includes a lateral component describing inhomogeneity of the atmospheric conditions due to the wide field of view of the real aperture radar imaging geometry. This model is purely empirical.	
Quadratic 2D Height	$\phi = \beta_0 + \beta_1 h + \beta_2 \theta + \beta_3 \theta r + \beta_4 h^2 + \beta_5 \theta^2$	Analogous to "Quadratic 2D Range" but replacing the slant range with elevation.	

observations and the test points, which can be used for the Kriging predictor.

If a bounded spatial variogram model $\gamma_{s,m}$ can be fit to the experimental variogram estimate, the value of the spatial covariance function at any spatial lag d is computed with [74]

$$C_s(d) = \gamma_{s,m}(\infty) - \gamma_{s,m}(d) \qquad (34)$$

where $\gamma_s, m(\infty)$ is the variogram sill, the value that the variogram attains at infinite spatial separation between the samples, which corresponds to the phase variance of the interferograms.

If the spatial statistics of the APS are estimated from the data, it is advisable to strive for a spatially homogeneous distribution of PS, such that a homogeneous distribution of lags d between the PS locations is achieved, ensuring a reliable estimate of the spatial variogram.

The imaging geometry of TRI should also be considered. Due to the limited antenna aperture size, the images are acquired on a polar grid. Thus, the data matrix as returned by the radar is defined on a polar grid in the range-azimuth plane (r, θ). For this type of sampling, the spatial lag d between two points must be determined using the distance formula for polar coordinates and not with the Euclidean distance normally used in most geostatistical packages.

In this article, a more efficient approach is used: the data are geocoded with a digital elevation model. The variograms are estimated on the geocoded data, which is now resampled in the 3-D Cartesian coordinates, where the distance between the points is easily determined.

This is relevant in the scenes with large variations in elevation, because distances in the slant-range azimuth grid could substantially differ from the ground distance between the points. This difference can hinder the fair comparisons of experimental variograms with theoretical covariance or semivariance functions derived from the turbulence theory.

C. Temporal Inversion

1) Temporal Covariance Model: Even after removing the APS estimate from the interferogram vector, considerable phase variability in time is observed in the residual interferometric phases [84], [85]

$$z_{\text{res}}(i, l) = z(i, l) - \hat{\epsilon}_{z, \text{atm}, s}(i, l) \qquad (35)$$

where $\hat{\epsilon}_{z, \text{atm}, s}$ is the regression-Kriging prediction of the spatially correlated APS, whose estimation is detailed in Section II-B.

Caudff *et al.* [84] reported the residual phase variation after correcting the APS by interpolating the spatially low-pass filtered phase observations of stable areas, a method similar

to the Kriging interpolation proposed in Section II-B, which does not use the spatial covariance structure of the APS in the prediction. In that case, the residual phases were observed to correlate with variation in the solar radiation.

Similar observations were made by Butt *et al.* [75], where after interpolating, the APS observed at a set of PS using IRF-K, a significant residual phase error was observed, especially for the areas with a low density of PS. This was explained through the short correlation length of the APS in space and its high temporal frequency.

Under the separable covariance model described in Section II-A, the residual APS in $z_{res}(i, l)$ is a realization of a Gaussian random process $\epsilon_{z,atm,t}$ with no spatial correlation and a temporal correlation matrix $\Sigma_{z,t}$, approximately the sum of a block diagonal matrix of APS and of a block-diagonal or diagonal matrix of noise contributions due to temporal decorrelation, as described in (25)

$$\Sigma_{z,res} \approx \mathbf{I} \otimes \Sigma_{z,atm,t} + \Sigma_{z,decorr,t}. \tag{36}$$

This formulation is not exact because of the sparse distribution of the PS across the scene and the approximated covariance obtained from the variogram; a residual spatial correlation of the APS can be expected. The residual error will increase with the increasing distance from the PS; for the sake of simplicity, this aspect has not been considered in this analysis.

If the noise in the corrected interferogram vector $\Sigma_{z,res}$ is assumed to be spatially uncorrelated, it is only necessary to consider the temporal correlation of APS and decorrelation in the solution of (5). In this case, the temporal covariance structure is described by a block-diagonal matrix $\Sigma_{z,res}$, and the sum of the temporal APS covariance and of the decorrelation covariance [see (36)].

Since $\Sigma_{z,res}$ is a block-diagonal matrix, i.e., the nuisance in $\mathbf{z}_{res}$ is not correlated across pixels, (5) can be solved separately for each of the P pixels, since $\mathbf{G}$ is a block-diagonal matrix of compatible size and shape, i.e., the displacement model does not include the spatial dependence of its parameters.

The temporal APS covariance $\Sigma_{z,atm,t}$ is estimated through $\Sigma_{y,atm,t}$ using an empirical temporal variogram, computed as the variance of the interferometric phases grouped by temporal baselines ΔT, as shown in Fig. 2

$$\gamma_t(\Delta T) = \frac{1}{2|N(\Delta T)|N_{PS}} \sum_{l=0}^{N_{PS}} \sum_{i \in N(\Delta T)} |z(l, i)|^2 \tag{37}$$

where $N(\Delta T)$ is the set of all interferograms with temporal baseline ΔT and z is the unwrapped interferometric phase.

Estimating the temporal covariance of the APS requires the computation of interferograms covering all temporal baselines up to a sufficiently long time-lag in order to fit a covariance model, even if only a subset of these interferograms can be employed for the inversion. This requirement is not as stringent, since only the interferometric phases at the PS are required, which are computed efficiently and are unaffected by temporal decorrelation.

Similarly, the covariance matrix of the decorrelation $\Sigma_{z,decorr}$ can be derived from the SLC covariance matrix $\Sigma_{y,decorr}$ [86] and the incidence matrix $\mathbf{A}$. In this article,

the approach suggested in [39] is used, assuming a Brownian decorrelation process as follows.

1) The interferometric coherence between two SLCs pixels $y(i, t_l)$ and $y(i, t_l + \Delta T)$ separated by a time ΔT is modeled with an exponential decay $\gamma(\Delta T) = \gamma_0 e^{-\Delta T/\tau}$. The observed coherence as a function of temporal baseline ΔT is computed by averaging interferograms with the same ΔT, giving $\hat{\gamma}(\Delta T)$. The parameters γ_0 and τ are estimated by minimizing $\left|\hat{\gamma}(\Delta T) - \gamma(\Delta T)\right|$ [67].

2) The model parameters are used to generate the coherence matrix of the SLC vector, Γ. Then, Γ is converted into the (incorrectly scaled) covariance matrix of the interferograms $\mathbf{z}$ using $\mathbf{A}$. For a pixel i

$$\Omega_{z,i} = \frac{1}{2} \mathbf{A} \Gamma_i \mathbf{A}^T. \tag{38}$$

3) Finally, Ω_z is rescaled to a covariance matrix using the observed interferometric coherences and the expression for the interferometric phase standard deviation of (16). For the ith pixel, the new matrix is

$$\Sigma_{z,decorr,i} = \mathbf{D} \Omega_{z,i} \mathbf{D} \tag{39}$$

where $\mathbf{D}$ is a diagonal matrix with the jth entry corresponding to $(\text{Var}[z_{j,i}]/\Omega_{z,i\,jj})$.

To improve the robustness of the estimated decorrelation covariance matrix and to reduce the computational load, γ_0 and τ are binned in 30 classes, and the average covariance matrix for each class is used in the inversion.

2) Pixelwise GLS Inversion: Thanks to the spatial correction of the APS described in Section II-B, the problem can be solved for each pixel individually using $\mathbf{z}_{res}$ instead of $\mathbf{z}$ to yield the estimate $\hat{\mathbf{p}}$ for all times $t_l, l = 1, \ldots, M$ at each location $\mathbf{s}_i$

$$\hat{\mathbf{p}}(i) = (\mathbf{G}^T \Sigma_{z,res}(i)^{-1} \mathbf{G})^{-1} \Sigma_{z,t}(i)^{-1} \mathbf{G} \mathbf{z}_{res} \tag{40}$$

where $\Sigma_{z,res}(i)$ indicates the ith block of $\mathbf{z}_{res}$ corresponding to the ith pixel.

The feasibility and robustness of the inversion described by (40) are controlled by the interplay of the available interferograms, determined by $\mathbf{A}$ and by the employed displacement model, and chosen by $\mathbf{p}$ through the design of $\mathbf{M}$.

In selecting $\mathbf{A}$ for the high repeat-interval observations of a fast-moving terrain, it is necessary to compromise between the computational and storage costs associated with the increasing number of interferograms and the unreliable phase information provided by the interferograms with large temporal baselines that are subject to low coherence and phase wrapping.

A conservative choice is to combine only consecutive SLC images in an *interferogram chain* [22], [25], [87], [88], so that the reference acquisition in the lth interferogram appears again as the slave of the $l+1$th interferogram. In this configuration, $N-1$ unique interferograms are produced.

An interferogram chain is convenient in combination with a displacement model assuming a constant velocity, i.e., $\mathbf{p} = \mathbf{v}$ with $\mathbf{v}$ a $P \times 1$ vector. In that case, phase contributions that appear once as a reference SLC and once as secondary SLC cancel each other in the GLS solution, leaving

This article has been accepted for inclusion in a future issue of this journal. Content is final as presented, with the exception of pagination.

BAFFELLI *et al.*: GEOSTATISTICAL ANALYSIS AND MITIGATION OF THE APSs

11

only the contributions from the interferograms at both ends of the chain [89].

Assuming a single velocity for the entire time-series negates the purpose of high repeat-rate TRI monitoring, because variations in displacement velocity over time cannot be estimated. The interferogram chain is also not suitable to estimate the full time-series of N velocities for each pixel, i.e., $\mathbf{M} = \mathbf{I}_{PN,PN}$ with $\mathbf{v}$ a PN-vector. This formulation likely results in unreliable estimates, because only one noisy interferometric phase observation is available for each model parameter.

Redundancy in the form of a simpler displacement model and of more interferograms can improve estimation robustness. Optimally, all possible $(N(N-1)/2)$ interferometric pairs can be used to obtain the maximum likelihood (ML) estimates of $(N-1)$ unwrapped differential phases [67], [86], [90] as if they were interferograms computed from a single master acquisition. These ML-estimate can then be converted into a displacement history with $N-1$ displacement relative to a virtual master.

This method is not applicable in the case presented in this article: the number of interferograms to compute and store would be too large. Other than these technical limitations, phase ambiguities and decorrelation also present an obstacle.

As to the former issue, assuming a maximum velocity of 2 m/day in the fastest parts of the glacier, phase wraps can be expected for interferometric pairs with a temporal separation of approximately 6 min.

Since the data are acquired with a repeat interval of 150 s, this allows wrap-free interferograms between the lth and the $l+1$th and $l+2$th SLC. Such large displacement velocities are not expected to be frequently observed; therefore, the requirement is relaxing by allowing a maximum temporal baseline of 500 s. This choice should not result in displacement-induced phase wraps except for the most severe surges in glacier velocity. This interferogram network is described by the following incidence matrix:

$$\mathbf{A} = \begin{bmatrix} 1 & -1 & 0 & 0 & 0 & \cdots & \cdots \\ 1 & 0 & -1 & 0 & 0 & \cdots & \cdots \\ 1 & 0 & 0 & -1 & 0 & \cdots & \cdots \\ 0 & 1 & -1 & 0 & 0 & 0 & \cdots \\ 0 & 1 & 0 & -1 & 0 & 0 & \cdots \\ 0 & 1 & 0 & 0 & -1 & 0 & \cdots \\ \vdots & \vdots & \vdots & \vdots & & \ddots & \end{bmatrix}. \quad (41)$$

The time-series is inverted using a displacement model assuming a constant velocity for a duration t_s longer than the SLC repeat interval. In this manner, the interferograms can be divided into *stacks*, where the displacement rate is constant. In this case, $\mathbf{M}$ is

$$\mathbf{M} = \mathbf{I}_P \otimes \begin{bmatrix} [1 & 0 & \cdots & 0]_{\times N_s} \\ [0 & 1 & \cdots & 0]_{\times N_s} \\ & & \vdots & \\ [0 & \cdots & 0 & 1]_{\times N_s} \end{bmatrix} \quad (42)$$

where N_s is the number of interferograms in each stack.

This model is a modified form of interferogram stacking [32], [34], [91], where a constant velocity for each pixel is assumed for the entire duration covered by the interferograms. In the modified model, N_s velocities are estimated, using the parameter to interpolate between the reliable estimates and temporal resolution. In this article, $N_s = 16$ is selected, corresponding to about 30 min.

III. DATA

A. Device: Ku-Band Advanced Polarimetric Radar Interferometer (KAPRI)

The data used in this article were acquired using a KAPRI [92], [93], a fully polarimetric version of the gamma portable radar interferometer II (GPRI-II) [94] and a Ku-Band portable terrestrial radar interferometer. The radar is based on the dechirp-on-receive frequency-modulated continuous-wave (FMCW) architecture [95]. With a chirp bandwidth of 200 MHz, a nominal distance resolution of 0.75 m is achieved. Since a windowing filter is used to suppress the processing sidelobes caused by the discrete Fourier transform (DFT) used for range compression, the effective range resolution is 0.9 m. Resolution in the direction perpendicular to the LOS is given by a 2-m-long slotted waveguide array with a half-power beamwidth of 0.385°, corresponding to a ground cross-range resolution of 7 m at 1-km slant range.

B. Bisgletscher 2015 Campaign

A series of KAPRI data spanning the period between July and late August 2015 was acquired from the Domhütte mountain hut at an altitude of 2940 m, looking at the Bisgletscher on the opposite side of the valley (see Fig. 3) and covering a range of distances between 4000 and 8000 m. At these distances, GPRI data have a cross-range resolution between 30 and 60 m and a range resolution of approximately 0.9 m. An SLC image was acquired every 150 s; the repeat time is chosen to minimize temporal decorrelation and to avoid phase wrapping due to the rapid motion of the glacier's surface estimated using the time-lapse camera to be as large as 2 m/day. The data set does not uniformly cover the duration of the measurement campaign due to a combination of the technical and logistical limitations.

1) The radar installation used the hut's electrical power supply, consisting of solar panels supplemented by a small hydroelectric plant. During the times of high activity at the hut, the radar had to be disconnected from its power supply. A buffer battery permitted continuing acquisition for approximately 6 h from the power cutoff. During longer interruptions, this alternative was not sufficient to ensure continuous operation.

2) Nearly 200 GB of SLC data was produced every day. To provide data download and control, the radar was connected to a Wi-Fi link provided by the PermaSense/X-Sense project [96]. Since this link is designed to connect a low-power sensor network, which is expected to produce a much lower daily data volume, daily transfers of the entire radar data set were not possible. Therefore, the SLC images were stored locally on a network-attached storage (NAS) system connected to the
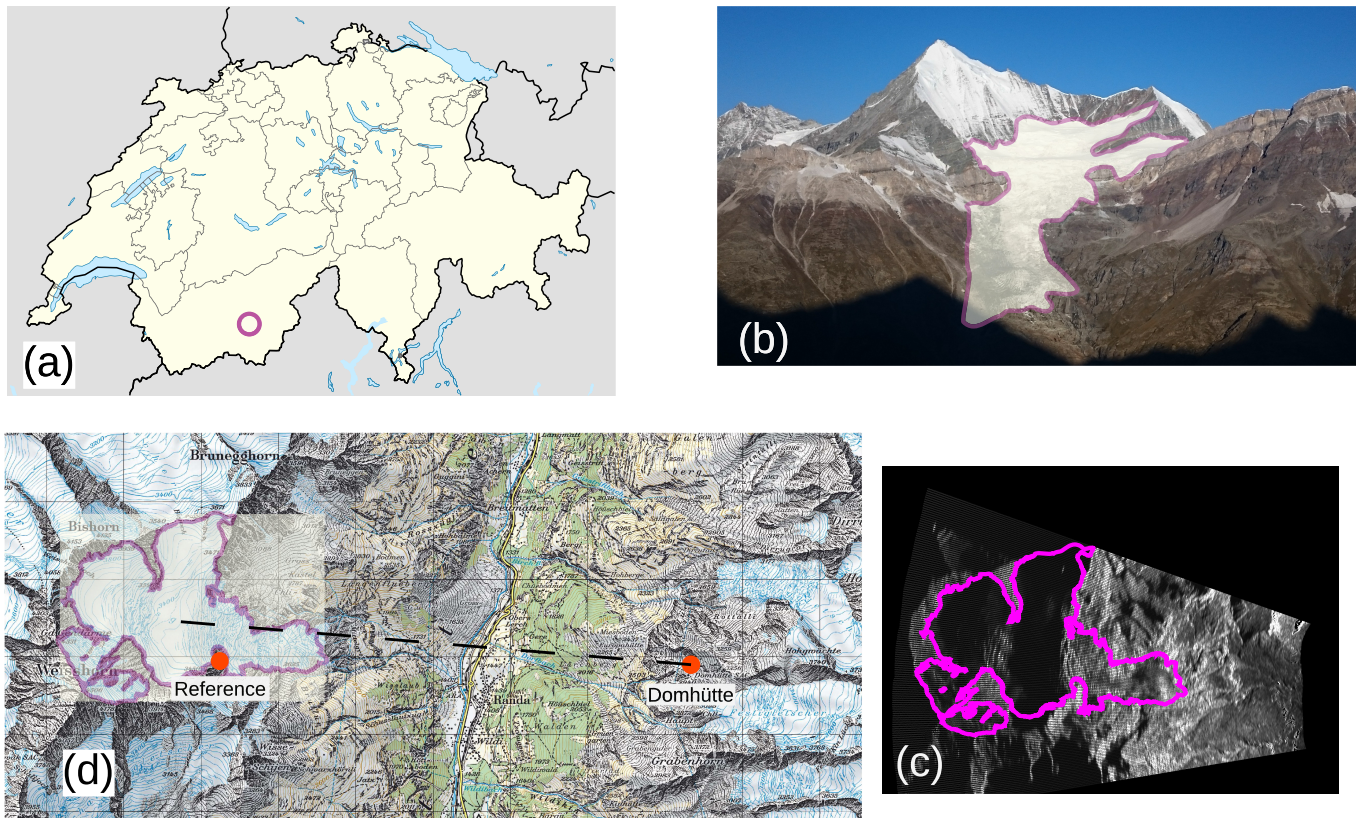
Fig. 3.   Overview of the area under study. (a) Approximate location of the Bisgletscher in the Canton of Valais, Switzerland. (b) Image of the Bisgletscher as seen from the radar point of view at Domütte, with glacier outline drawn in purple. (c) Geocoded average backscatter power map geocoded in Swiss map coordinates. (d) Locations of radar at Domhütte, glacier, and reference location for interferogram referencing overlaid on a topographic map with 1 : 50000 scale. (Basemap: [97]).

radar using a local-area-network connection. Since only a 100-MB/s Ethernet cable was installed, the maximum daily data amount that could be transferred from the radars own storage to the NAS was still smaller than the predicted daily amount. To avoid running out of storage space on the computer controlling the radar, acquisitions were only carried out for 12 h each day, while the remaining time was dedicated to copying the data to the NAS system.

From the acquired data, a subset of data is sampled for the analysis of the APS: ten timestamps are chosen randomly from the set of acquisitions. For each of these timestamps, all SLCs closer than 1 h are used for the analysis. The random sampling is used to ensure that different atmospheric conditions are represented in the study, since they are presumably influenced by the weather and time of the day.

C. Data Processing

The acquired SLCs are coregistered to a common master acquisition by amplitude cross correlation to minimize the loss of coherence. Interferograms are formed by complex multiplication, followed by 5×2 multilooking. A larger range multilooking is used in order to minimize the loss of azimuth resolution, which by virtue of the acquisition geometry increases linearly with slant range distance. Interferograms

are unwrapped using the minimum cost flow unwrapping algorithm and referenced to a reference point corresponding to a stable rock face close to the glacier, as shown in Fig. 3.

The PSs used to derive the spatial and temporal statistics were detected using the intensity-mean-to-standard-deviation ratio [50] on an SLC stack of 50 acquisitions and by removing the PS found in the areas known to be moving. The initial list of candidate PS was reduced to an approximately homogeneous spatial PS density using the method described in [98], employing the interferometric coherence with respect to the first SLC in the stack as a quality measure. The processing chain is implemented using Python, R, and the Gamma Software on top of the Nextflow [99] dataflow programming framework, which allows a reproducible analysis of the time-series.

IV. RESULTS

A. Spatial Correction of APS

1) Selection of Stratified APS Model: As discussed in Section II-B, the APS in the interferograms is modeled as the sum of a deterministic delay predicted by an atmospheric stratification model and a turbulent atmospheric delay contribution, modeled as a Gaussian random variable.

To select the best performing linear model for the stratified APS $\epsilon_{z,\text{atm, strat}}$, a statistical model comparison is made on a

This article has been accepted for inclusion in a future issue of this journal. Content is final as presented, with the exception of pagination.

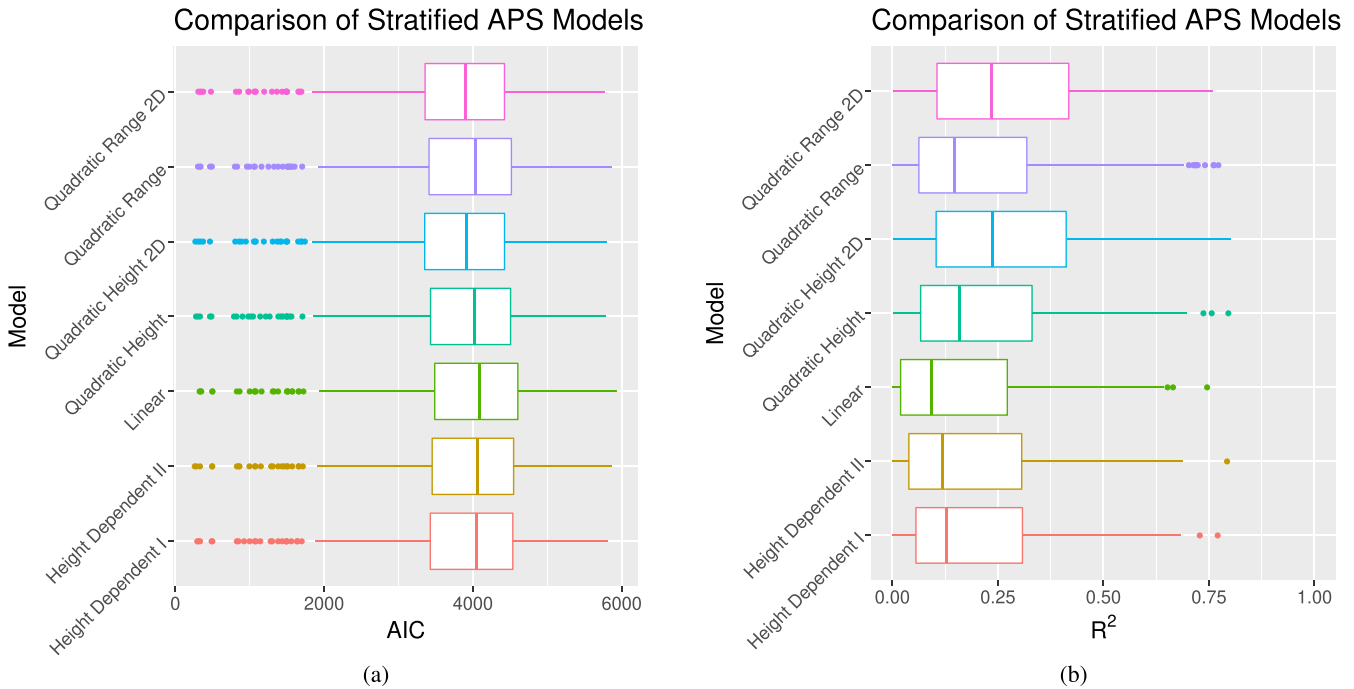BAFFELLI *et al.*: GEOSTATISTICAL ANALYSIS AND MITIGATION OF THE APSs

13

Fig. 4.   (a) Boxplot of the AIC values for a selection of models described in Table I. To produce this figure, 508 interferograms were considered. Each of the models discussed was applied to every interferogram, and the AIC statistic was computed. The AIC is plotted as a color-coded histogram, and the model whose AIC is lower is the one whose performance is the best relative to the other models it is compared with. (b) Boxplot of the R^2 values for the models listed in Table I. The plot is obtained with the same procedure as in (a).

large set of interferograms. For each interferogram l at time t_l in the network, an OLS estimate for $\beta(t_l)$ is computed for every linear model among those described in Table I.

The model fit parameters $\beta(t_l)$ alongside summary statistics, such as the sum of residuals, the R^2 value, and the AIC [80] are stored for each model run. The results of numerical evaluation are shown in Fig. 4(a) as a boxplot of the AIC values grouped by the model; each model is assigned a different color in the bar plot. A statistical summary of R^2 values is shown in Fig. 4(b) using a similar visualization.

2) Spatial Covariance Model for Turbulent APS: The spatial correction of the APS contribution is performed by predicting the unobserved APS at the locations of interest **s** according to the regression-Kriging equation (32). The estimated APS is then subtracted from the interferogram as in (35). The prediction at a point $\mathbf{s}_i$ requires the spatial covariance of the APS between this point and the PS used as observations.

As the true APS covariance is not known, it is replaced with a covariance model derived from an experimental variogram, as illustrated by (34). The variogram is computed by averaging the individual spatial variograms obtained from a number of interferograms, according to (33). These interferograms are generated using 100 SLC acquisitions, from which all PS interferograms with a maximum temporal baseline of 120 minutes are formed.

The spatial variograms obtained from each interferogram are plotted as dots in Fig. 5(a), and their color encodes the temporal baseline. Assuming the validity of the separable covariance, there should be no variation in spatial covariance between the interferograms; this is tested empirically by plotting the standard deviation of the spatial variograms across realizations,

shown in Fig. 5(a) as the gray ribbon around the averaged variogram and plotted as a black dashed line. An exponential variogram model, shown as a blue line, is fitted to the average.

3) Performance of Spatial APS Removal: The performance of the spatial APS estimation is assessed by cross-validation. A second set of PS was located on stable areas around the glacier, excluding those used for the regression-Kriging prediction. The phases of each interferogram and the residual phase after the removal of the APS estimates at these points are extracted and converted into velocities.

The results of cross-validation are displayed as histograms in the *no* row of Fig. 6. Three methods are compared. The regression-Kriging is shown in the column labeled *kriged*. The reference case with no correction applied is displayed in the column *unprocessed*, while the results after removal of the stratified APS contribution are shown in the column labeled *lm*. The interferometric phases outside of the glacier correspond to the APS only, because on rocks, no displacement is expected at the scale of the interferogram's temporal baseline. Therefore, the distribution of the estimated velocities on PS can be used as a proxy for the APS-correction quality.

A visual comparison of these methods, in the form of standard deviation maps, is shown in the first row of Fig. 9(a)–(c) for the uncorrected case, the stratification model, and regression-Kriging, respectively. These maps are obtained with a sample estimator for the standard deviation, applied on the estimated velocity time-series.

A more quantitative assessment of the standard deviation of these residuals is given by the summary statistics Table II in the rows labeled "no." The table shows the bias and standard

This article has been accepted for inclusion in a future issue of this journal. Content is final as presented, with the exception of pagination.

14   IEEE TRANSACTIONS ON GEOSCIENCE AND REMOTE SENSING

(a)   (b)
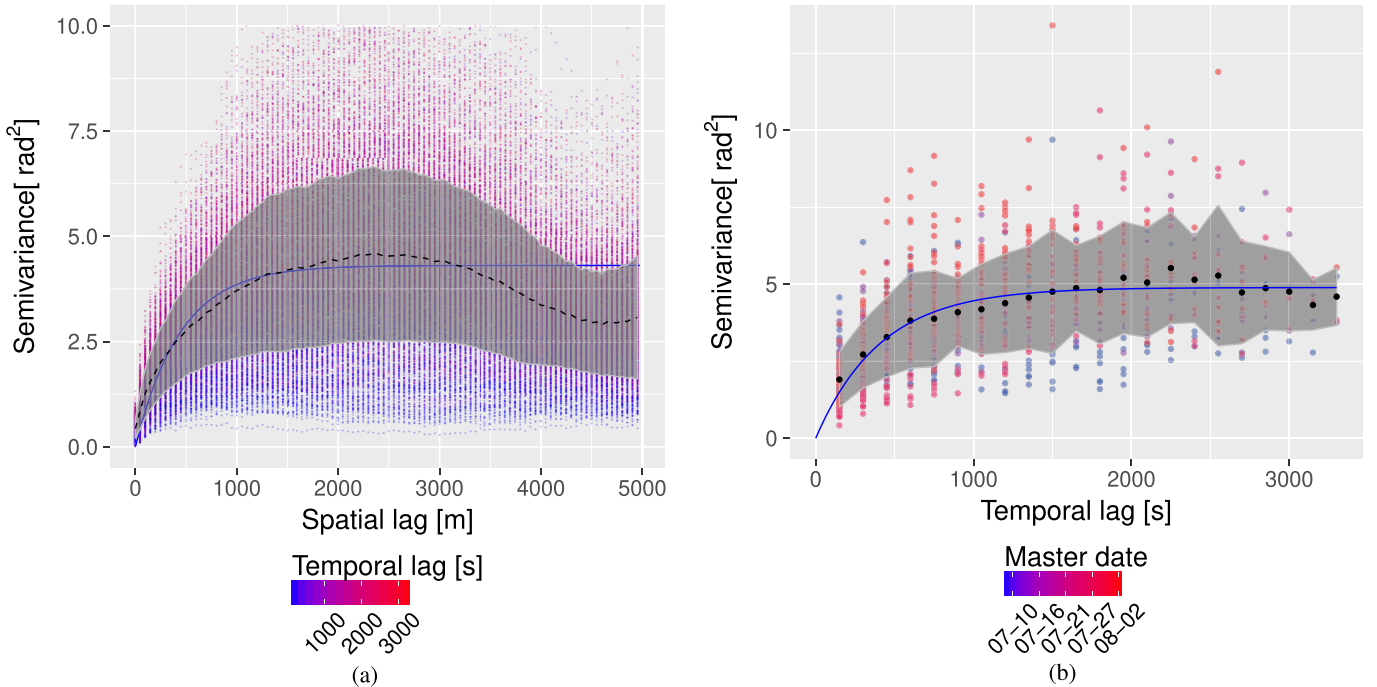
Fig. 5. Spatial and temporal variograms derived from 1535 PS interferograms computed from 100 SLC acquisitions. All distinct interferograms up to a maximum temporal baseline of 120 minutes were computed and unwrapped. (a) Empirical spatial variogram. Each dot corresponds to the empirical spatial variogram for one PS interferogram, and its color indicates the temporal baseline of that interferogram. The black line is the mean variogram, surrounded by a gray ribbon showing the standard deviation of the individual variograms, while the blue line shows the fitted exponential variogram used to compute the Kriging predictions. (b) Empirical temporal variogram, computed as the phase variance of the PS interferograms with increasing temporal baselines. The color of the dots encodes the date of the master SLC used in computing that interferogram, the black dots show the mean variogram over the set of all interferograms, and the gray ribbon is its standard deviation. The blue line shows an exponential variogram model fit, which is used to generate the temporal covariance matrices used in inversion.

TABLE II

BIAS AND STANDARD DEVIATION OF THE RESIDUAL DISPLACEMENT RATE IN m/day EXTRACTED FROM A SET OF PS LOCATED OUTSIDE OF THE GLACIER AND ASSUMED NOT TO BE UNDERGOING DISPLACEMENT

Method	Stacking approach	Bias	Standard deviation
kriged	OLS	$-4.11 \cdot 10^{-3}$	$5.8 \cdot 10^{-2}$
kriged	APS+Coh	$-2.82 \cdot 10^{-3}$	$5.48 \cdot 10^{-2}$
kriged	Coh	$-2.67 \cdot 10^{-3}$	$5.76 \cdot 10^{-2}$
kriged	APS	$-1.99 \cdot 10^{-3}$	$5.43 \cdot 10^{-2}$
kriged	no	$-1.06 \cdot 10^{-3}$	0.26
lm	no	$1.96 \cdot 10^{-2}$	0.96
unprocessed	no	$4.9 \cdot 10^{-2}$	1.44
unprocessed	OLS	$5.04 \cdot 10^{-2}$	0.49
lm	OLS	$5.25 \cdot 10^{-2}$	0.49
unprocessed	APS	$5.38 \cdot 10^{-2}$	0.47
lm	APS	$5.62 \cdot 10^{-2}$	0.46
unprocessed	APS+Coh	$6.76 \cdot 10^{-2}$	0.47
lm	APS+Coh	$7.17 \cdot 10^{-2}$	0.47
unprocessed	Coh	$8.89 \cdot 10^{-2}$	0.47
lm	Coh	$9.74 \cdot 10^{-2}$	0.47

deviation of the displacement estimates and calculated over all times and locations.

B. Temporal Inversion

As explained in Section II-C, it is assumed that the APS correction using regression-Kriging removes the spatial correlation of pixels; only the temporal correlation of pixels

along the stack, attributed to the residual APS, described by $\Sigma_{z,atm,t}$, and the decorrelation, described by $\Sigma_{z,\text{decorr}}$, must be considered in the GLS inversion, which can now be performed pixel by pixel.

1) Temporal Covariance Model: The Brownian coherence decay model parameters τ and γ_0 were computed using a subset of the interferograms. These estimates are useful to quantify the rapidity of the decorrelation process and are used to construct the covariance matrix $\Sigma_{z,\text{decorr}}$, as described in Section II-C. The estimates of γ_0 and τ are plotted as geocoded maps overlaid on a topographic map in Fig. 7.

The second component of the temporal covariance is the covariance of the APS, assuming that the spatiotemporal separability of the APS statistics $\Sigma_{y,\text{atm},t}$ is estimated from a temporal variogram using a set of PS interferograms with the increasing temporal baselines. Using this method, the variogram at lag t corresponds to the phase variance computed for all interferograms with a temporal baseline t, as shown in Fig. 2. The resulting temporal variogram is shown in Fig. 5(b) along with a curve showing the fitted exponential variogram model.

2) Performance of Pixelwise GLS Inversion: The pixelwise GLS inversion performance is tested by the same cross-validation procedure described in Section IV-A. The phases at the same set of points described above are extracted, converted in displacement velocities, and shown in Fig. 6, in the rows named *OLS*, *Coh*, *APS + Coh*, and *APS* that

This article has been accepted for inclusion in a future issue of this journal. Content is final as presented, with the exception of pagination.

BAFFELLI *et al.*: GEOSTATISTICAL ANALYSIS AND MITIGATION OF THE APSs
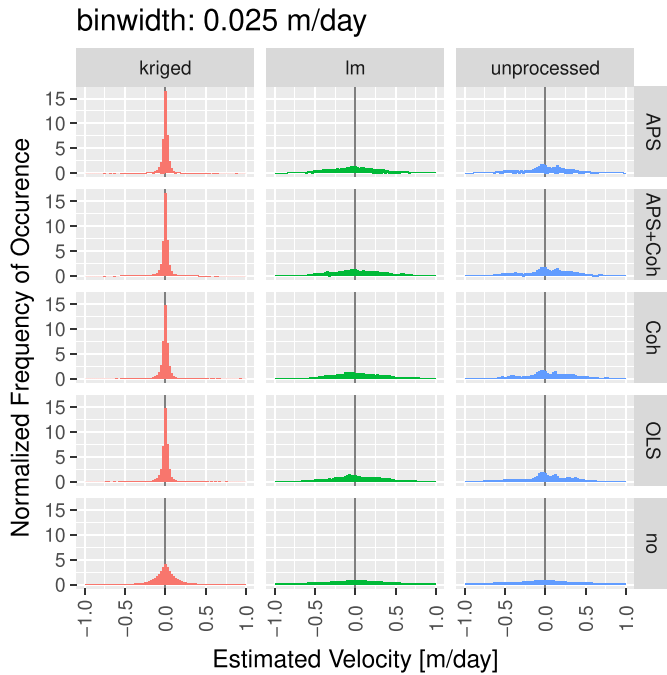
15

binwidth: 0.025 m/day

Fig. 6. Histogram of the estimated velocities at the nonmoving location for different combinations of APS correction and time-series inversion methods. Each column corresponds to a spatial APS correction method: *kriged* is obtained using regression-Kriging, *lm* using the stratified APS only, while in the column *unprocessed*, no spatial APS correction is applied. Across rows, different temporal covariance models are used for the GLS time-series inversion. In *APS*, only the temporal covariance of the APS is considered; in *Coh*, only the covariance of the temporal decorrelation process is considered, while *APS + Coh* uses both. In *OLS*, no covariance model is used, while in *No*, the interferometric phases are converted into velocities.

represent four inversion approaches using different temporal covariance matrices.

1) *OLS:* OLS inversion—the temporal covariance matrix is set to the identity matrix.
2) *Coh:* GLS inversion—temporal covariance only includes the Brownian decorrelation model.
3) *APS:* GLS inversion—temporal covariance only includes APS.
4) *APS+Coh:* GLS inversion—temporal covariance according to (36).

The same plots are repeated across three columns (*Kriged*, *LM*, and *unprocessed*), showing the combined effect of different spatial APS removal techniques and temporal covariance models.

The average velocity at the nonmoving location is expected to be close to zero with a small variance, as they are derived from the interferometric phases of the scatterers that do not displace significantly at the timescales of the interferometric baseline. Therefore, larger variances indicate a larger uncorrected APS contribution or a higher level of decorrelation causing more phase noise.

An estimated velocity map is shown in Fig. 8 for a small group of times. Three maps obtained without spatial APS correction and using a pixelwise OLS inversion are shown in Fig. 8(a). The same maps obtained with regression-Kriging and an OLS inversion are shown in Fig. 8(b). Finally,

in Fig. 8(c), regression-Kriging is combined with GLS using a temporal covariance considering both APS and decorrelation.

The temporal standard deviation of the estimates is shown in Fig. 9(d)–(i).

V. DISCUSSION

A. Spatial Correction of APS

1) Selection of Stratified APS Model: The stratified APS contribution is predicted by a linear model. It is hard to know *a priori* which of the models listed in Table I is the most suitable to the situation analyzed in this article.

Model selection was made using a statistical comparison, as described in Section IV-A. Fig. 4(a) shows a statistical summary of the AIC values, while Fig. 4(b) shows a similar summary of R^2 values.

The AIC values are only meaningful in the relative sense: among the investigated models, the one with the lowest AIC will have the best fit quality, in the ML sense [80]. As shown by the Box plot in Fig. 4(a), all models have a very similar distribution of the AIC values over the interferograms considered for the analysis, with the "Quadratic Height 2D" model showing the best AIC and the higher R^2 in Fig. 4(b).

The similar distributions of the AIC statistics across the models are perhaps caused by multicollinearity between the slant range distance and the height variables in the linear regression, which is explained by the observation geometry shown in Fig. 3: an increase in distance from the radar corresponds to increasing terrain elevations. The presence of multicollinearity is verified empirically in Fig. 10 by plotting r against h for the points used in regression. The possibility of multicollinearity seems realistic considering the correlation of r and h. In this case, either regressor can be included in the stratified APS model.

The 2-D model including height and azimuth angle was chosen for regression-Kriging as it shown the highest R^2 in Fig. 4(b).

The inclusion of the azimuth angle presumably increases the model fit quality, because it can describe the lateral variations in the APS due to the wide field of view of the radar. Despite this, it only achieves a median R^2 of 0.25 and an interquartile range of 0.3. This means that for most interferograms, between 80% and 60% of the total phase variability is not explained by stratification.

Considering the initial assumption of the APS being the superposition of stratification and turbulence, this result means that a majority of phase variability should be attributed to other processes—likely turbulence—highlighting the importance of statistical modeling.

The underwhelming performance of the APS stratification models is also seen in Table II in the row where "Method" is "lm" and "Stacking Approach" is "no." Compared with the uncorrected case, shown in the very last row of that table, the estimation standard deviation is reduced by only 0.4 m/day, but is still of a magnitude comparable with the glacier's daily displacement.

These results are in contradiction with several studies of APS correction in TRI [31], [41]–[47], [56], where a
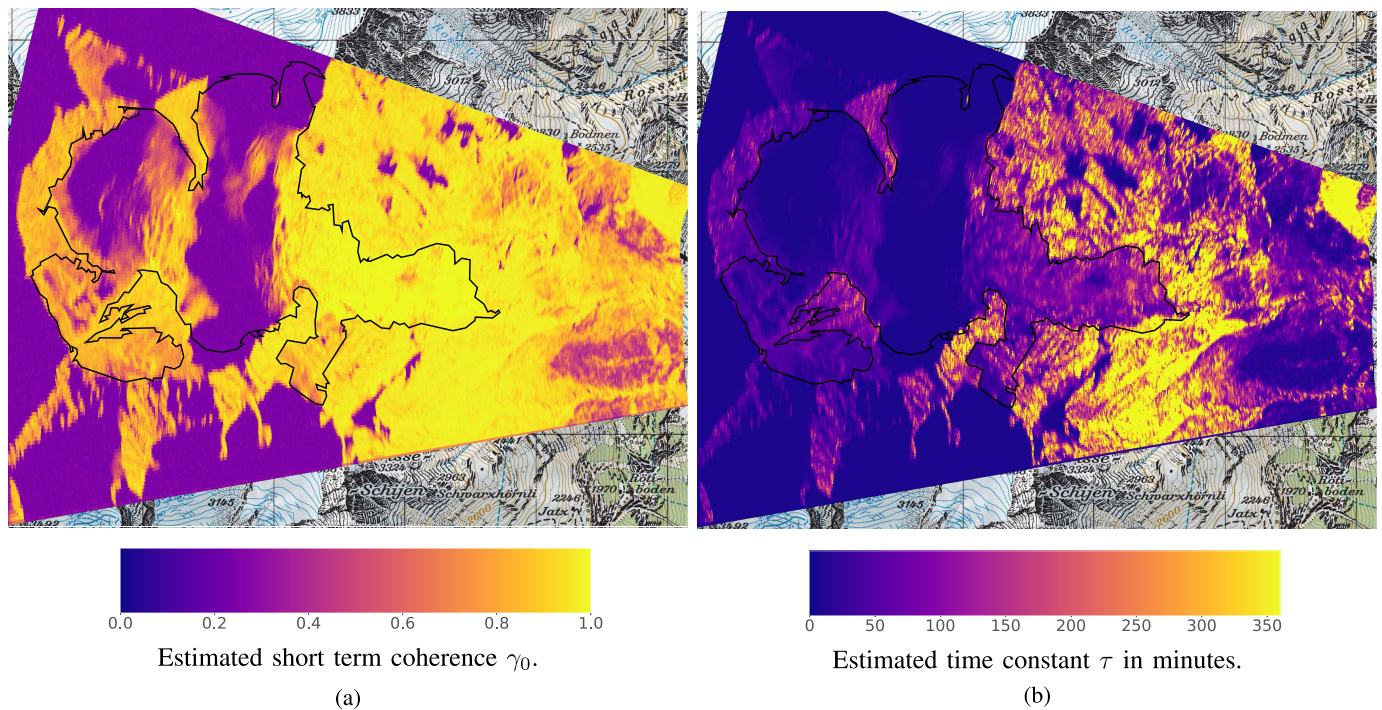
Fig. 7. Estimated (a) short-term coherence γ_0 and (b) time constant τ parameters for the Brownian coherence decay model $\gamma(\Delta t) = \gamma_0 e^{\Delta t/\tau}$. The data were obtained by fitting an exponential decay on average coherence maps binned by temporal baseline. The outline of Bisgletscher is shown as a black polygon. (Basemap: [97]; swisstopo; outline: [100].)

stratification model is shown to reduce significantly both bias and variance. However, these studies were sometimes performed in less-challenging environments and for the purpose of monitoring slower displacements, in most cases using a single reference interferogram network.

In [41], a single reference interferogram network was considered, where interferograms are computed with respect to one master acquisition, with the purpose of detecting very small displacements. In that case, the scene under study was located at distances between 0 and 1400 m from the radar; thus, the total propagation path is almost 1/8 of the path observed in the Bisgletscher scenario.

Similar considerations apply to [42], where the scene under study is located much closer to the radar and interferograms are computed with respect to a single reference acquisition. The scenario considered in [44] and [56] is again similar, since a single-reference interferogram network is considered and the radar-scene distance is once more significantly smaller than that in the Bisgletscher study. A similar situation is considered in [45] and [46].

A single-reference interferogram network means that with increasing temporal baselines, the effects of global or low-spatial-frequency changes in the atmospheric propagation speed become appreciable. This can be explained as follows: weather-driven changes in the atmospheric water content and especially changes the atmospheric pressure—the hydrostatic delay—are presumably of lower spatial frequency than the turbulent structures.

Moreover, these large-scale offsets are not likely to vary at the timescale of the radar's repetition rate, in the order of 2 min for the present case study. Therefore, for short temporal base-

lines, the magnitude of the phase delay caused by turbulence—mostly associated with turbulent mixing of wet air, the *wet delay*—may be stronger than the stratification signal.

In contrast to these studies, Dematteis *et al.* [47] computed interferograms between subsequent acquisitions. He reported a good performance of the stratification model fit; however, the author is using a longer repeat time of 16 min, almost eight times as large as the one employed for the observation of Bisgletscher. Other than this difference in the temporal baseline, the observation geometry is different, as in the former case, the radar is looking upward from a much lower elevation (1500 m) toward the glacier located at higher altitudes, while in the latter, the glacier is observed from almost the same elevation as the glacier's center but with the propagation path crossing a valley.

2) Covariance Model for Turbulent APS: In Fig. 5(a), the individual spatial variograms obtained from a number of PS interferograms are shown as dots colored by the temporal baseline. Under the separable covariance model, increases in the temporal baseline can only scale or offset the spatial variogram and not modify its shape [101].

In the experimental variograms, the shape changes with the increasing temporal lags, as shown by the different shapes of the upper and lower ranges of the standard deviation ribbon plot. With the increasing temporal lags, an oscillation in the middle at 2500-m lag is visible; this type of periodic structure of the variogram is likely a combination of the *hole effect* [102], which is observed for spatially periodic structures, and of the anisotropy in the spatial correlation structure of the APS.

Moreover, the variation in the spatial variogram shape as a function of temporal lags indicates the possibility of

This article has been accepted for inclusion in a future issue of this journal. Content is final as presented, with the exception of pagination.

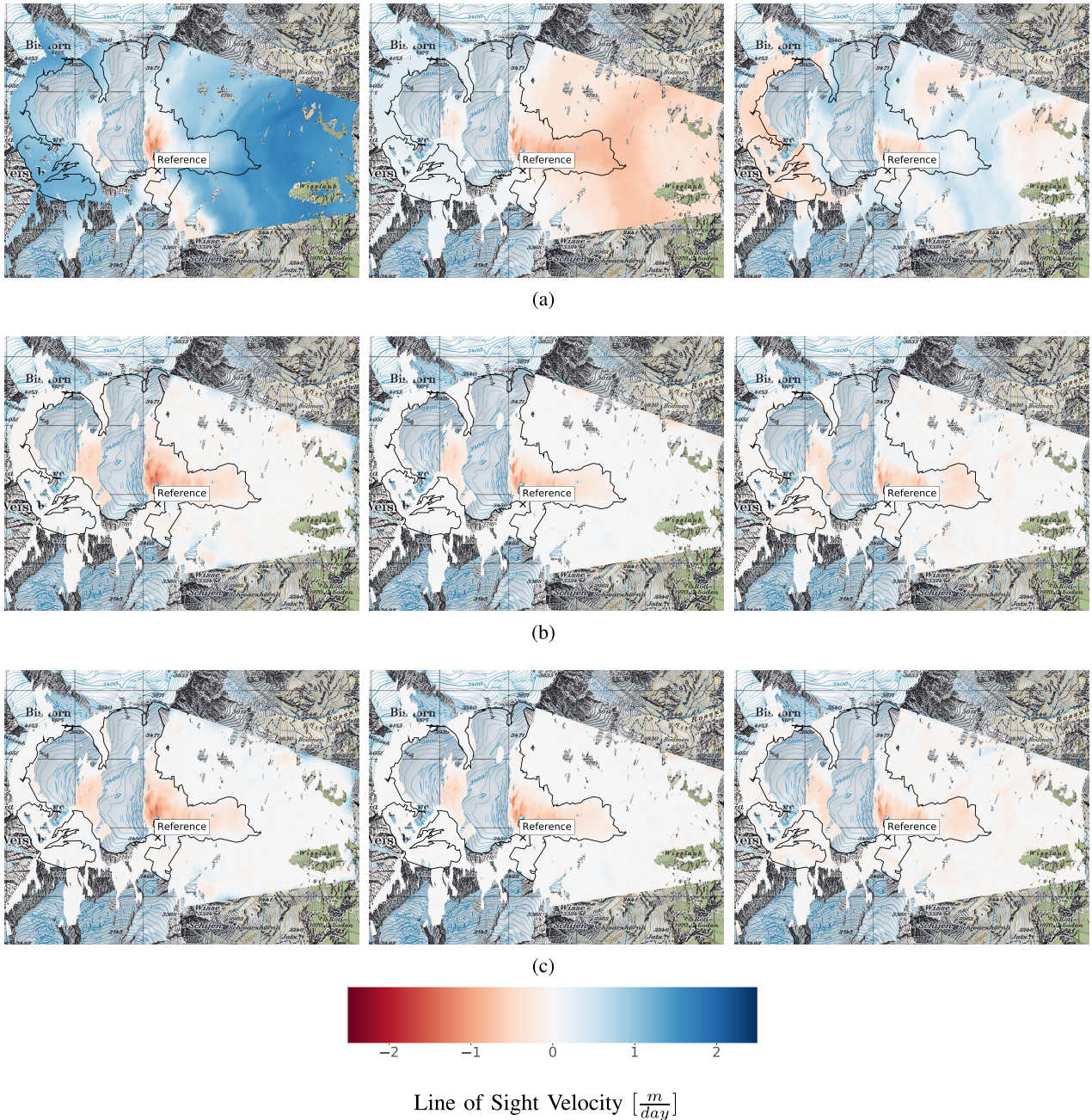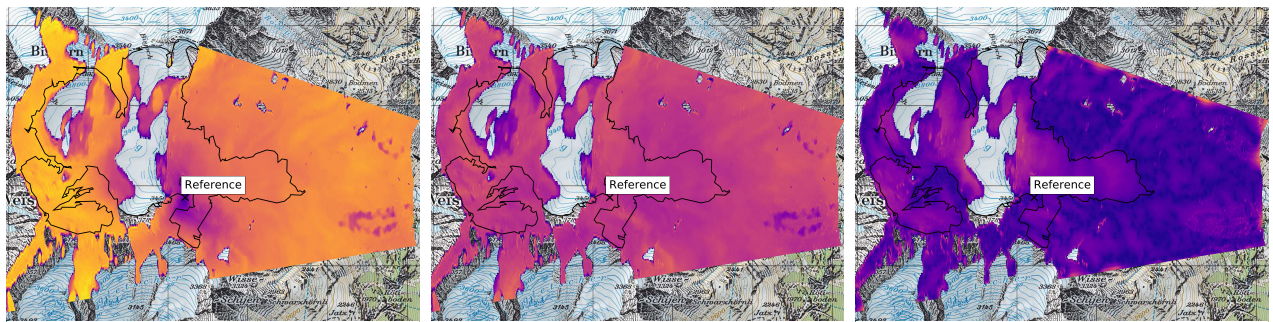BAFFELLI *et al.*: GEOSTATISTICAL ANALYSIS AND MITIGATION OF THE APSs

17

Fig. 8. Time-series of the estimated velocity maps for a subset of times. (From left to right) July 14 2:33, July 26 16:32, and August 2 11:36, central European summer time (CEST). (a) No spatial APS correction and OLS solution for the velocity. (b) Spatial APS correction using regression-Kriging combined with OLS inversion. (c) Spatial APS correction using regression-Kriging and velocity inversion with full covariance model (APS and decorrelation). The outline of Bisgletscher is shown in black. (Basemap: [97]; outline: [100].)

space–time interactions. Given the relatively short repeat interval, it is not surprising that these interactions may happen. A classic example is Taylor's hypothesis [33], [68], where turbulent structures are transported by the wind without changing their shape.

Despite the variability, suggesting instationarity, a separable covariance model is still chosen as an approximation because of its lower computational cost. Under this model, only one spatial covariance function needs to be fit to the average of individual spatial variograms. This function can be used to predict the unobserved APS in all interferograms.

The average variogram is shown in the plot as a black dashed line; the blue line shows an exponential variogram fit. The average spatial variogram shows again the same oscillation that was observed in the individual variograms, especially in those at larger temporal lags. This is likely a sign of periodic structures in the APS or of anisotropies. The former could be caused by the phase unwrapping error, while the latter suggest that a more comprehensive variogram model including anisotropy could result in a better fit [103], [104].

A more sophisticated approach to spatial covariance modeling has been suggested [75], where instead of stationary,

This article has been accepted for inclusion in a future issue of this journal. Content is final as presented, with the exception of pagination.

18   IEEE TRANSACTIONS ON GEOSCIENCE AND REMOTE SENSING

(a) No Spatial APS correction.   (b) Spatial APS correction with stratified   (c) Spatial APS correction using
                                        model.   regression-Kriging.
                    The velocity in this group of maps was estimated from individual interferograms.
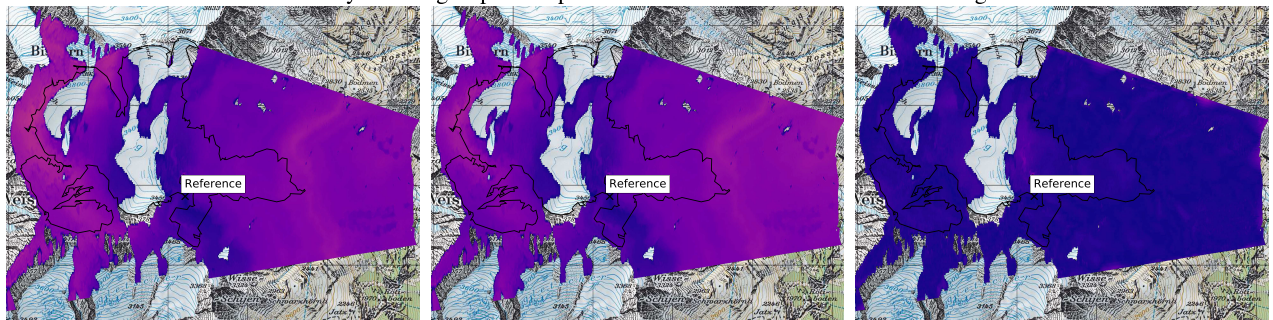
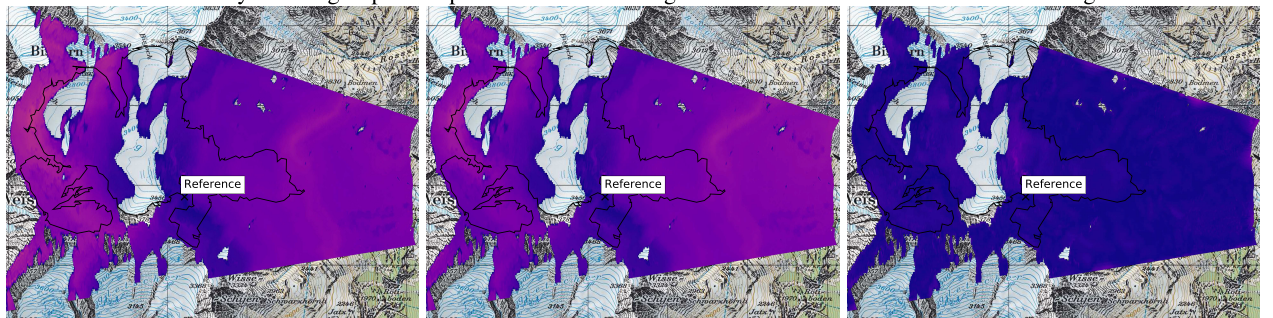(d)   (e)   (f)
        The velocity in this group of maps was estimated using OLS inversion on the corrected interferograms.

(g)   (h)   (i)
The velocity in this group of maps was estimated with GLS inversion and a temporal covariance model considering APS and decorrelation.

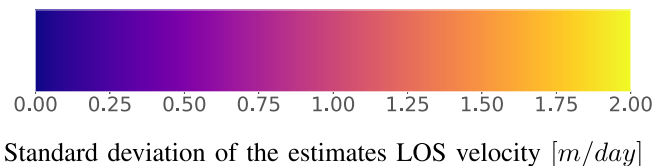Standard deviation of the estimates LOS velocity $[m/day]$

Fig. 9.   Standard deviation maps of the velocity estimates for different combinations of APS correction and velocity inversion methods. (From left to right) No correction, stratified APS model, and regression-Kriging. From top to bottom: velocities estimated from single interferograms, OLS inversion, and GLS inversion with the *APS + Coh* covariance model. (Basemap: [97].) (a), (b), and (c) Velocity estimate from single interferograms with (a) no APS correction, (b) stratification model, (c) regression-Kriging. (d), (e), and (f) Velocity estimated using OLS timeseries inversion on a stack of interferograms corrected as in (a), (b), and (c), respectively. (g), (h), and (i) Velocity estimated with GLS timeseries inversion on a stack of interferograms corrected as in (a), (b), and (c), respectively.

isotropic covariance functions, the author proposed to use IRF-k to fit nonstationary, anisotropic covariance functions. The authors used this method to extrapolate the observed APS from the PS to the rest of the scene.

In the case study presented by Butt, performed on another interferometric time-series of the same Bisgletscher scene, only an isotropic—albeit instationary—covariance function was used in the interpolation.

3) Performance of Spatial APS Removal: The performance of APS prediction and removal is evaluated in Fig. 6 in the figure row named *no*. This is obtained by plotting the histogram of the velocity estimates derived from the corrected interferogram, evaluated at stable areas, as described in Section II-B.

If no spatial APS correction is applied (column *no* of Fig. 6 and the last row of Table II), a large bias and standard deviation
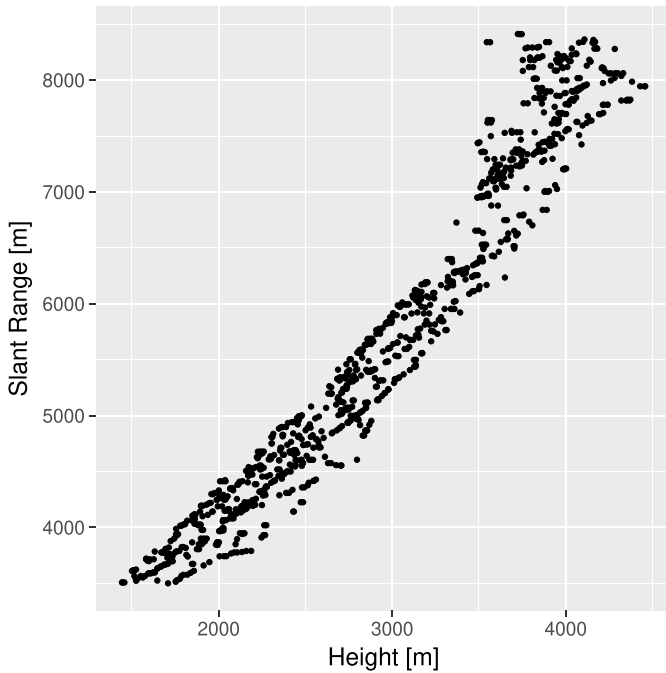
Fig. 10. Scatterplot illustrating the correlation between the slant range (r) and height (h) used as regressors for several models of atmospheric stratification listed in Table I.

are observed. The latter is almost as high as one half of the expected maximum displacement of the glacier's surface. If no correction of the APS is applied, the estimated displacement will be unreliable.

The large error variance is also visible in the standard deviation map in Fig. 9(a). Interestingly, a minimum in standard deviation is observed in the vicinity of the reference point. This is because referencing the phase is able to mitigate part of the APS thanks to its spatial correlation.

By subtracting an estimate of the stratified APS (column *lm* of Fig. 6 and the second-to-last rows of Table II) a reduction in phase variance is visible in comparison with the uncorrected interferograms. However, the standard deviation of the estimates is only reduced by one-third, as shown in the summary statistics of Table II. This is also appreciated in Fig. 9(b), where the overall variance is reduced. The latter result is consistent with the poor performance of the stratified APS model, as no model was capable to explain more than 30% of the phase variance of the APS. This is observed in the R^2 plot of Fig. 4(b). Thus, most of the observed phase variation should be attributed to the turbulent APS or to other unmodeled phase nuisances.

Compared with the uncorrected case, the subtraction of the regression-Kriging estimates (column *kriged* of Fig. 6 and row "kriged, no" of Table II) of the APS reduces the standard deviation by three-quarters.

In Fig. 9(c), the standard deviation is lower overall: now instead of using a single phase reference as in the uncorrected reference case, a set of phase references—the locations of the nonmoving PS—is used to extrapolate the APS using the estimated covariance function.

An area of high estimation variance is still observed in the center of the scene at the location of Bisgletscher. A part of this variance is presumably due to natural variations in the glacier's surface speed. The remaining variance is the inherent regression-Kriging prediction variance, which increases with the increasing distance between the observations at the PS and reconstruction locations.

In the case of the glacier, the average distance between the pixels on the glacier surface and the nearest PS is larger than that in the rest of the scene. A similar pattern was seen in the theoretical variance maps obtained during the regression-Kriging procedure.

A similar APS correction performance is observed in the IRF-k approach described by Butt *et al.* [75]. This result is expected given the fact that intrinsic random functions are comparable with regression-Kriging if the covariance function is estimated accounting for the nonstationarity [78], which is partly obtained by removing the stratification trend before variogram estimation.

B. Temporal Inversion

1) Temporal Covariance Model: The temporally correlated noise in the interferogram phase vector is modeled as the sum of a residual APS and the phase noise due to decorrelation. The latter is described with a Brownian motion model, attributed to the random motion of many scatterers in each resolution cell, resulting in an exponential decay of the interferometric coherence γ.

The estimated exponential decay parameters are shown in Fig. 7. A very widespread of the decorrelation time constant τ is noticeable in Fig. 7(b), probably due to the variety of surfaces types, ranging from rocks to forests and glaciated areas. Of interest in this analysis is the surface of the glacier, outlined by the black polygon.

There, a time constant between 5 min and 2 h is observed. This ensures reliable interferometric phases up to the temporal baselines of approximately 1 h for the slower decorrelating areas, assuming a minimum coherence threshold of 0.6. Given the high probability of displacements producing phase wraps, it is not advisable to include interferograms with large temporal baselines in the time-series inversion.

On the other hand, the spatial variability in the short-term coherence γ_0, which roughly corresponds to the mean coherence at the shortest temporal baseline of 150 s, is lower [see Fig. 7(a)]. Areas that show a short-term coherence loss correspond to vegetation and regions of low backscatter intensity. The estimate over the glacier's tongue displays high coherence, suggesting the suitability of the chosen repeat time of 150 s for the study of its displacement.

The other component of the temporal covariance matrix is represented by the temporally correlated contribution of the APS, which is estimated by an empirical variogram, as discussed in Section II-C. The experimental variogram is displayed in Fig. 5(b); it appears that the semivariance rapidly increases and settles at 90% of the sill after about 500 s, such that, after this time, the APS can be effectively considered uncorrelated. However, significant variability is observed

between the variograms computed at different dates (represented as different colors in the plot), presumably reflecting the large variability in propagation conditions related to weather changes.

The rapid settling of the vaiogram at the sill is in contrast with the observation made by Iannini and Monti Guarnieri [56], where the semivariance was observed to increase up to a time lag of 5 days before settling to a sill. The observation conditions were significantly different in that case, since the targets of interest were much closer to the radar (600 m versus 8 km for the Bisgletscher data set) and measurements were performed at lower elevations. Moreover, the variograms in that work were estimated without removing the stratification trends, thus possibly explaining the longer correlation time—up to five days—claimed by the authors.

This result suggests that the APS is not significantly correlated with time at the timescales of the acquisition rate of 2.5 min. Specific experiments—for example, by observing a single location at a high repeat interval—would be necessary to better estimate the decorrelation time of the APS.

2) Performance of Pixelwise GLS Inversion: When both components of the temporal covariance matrix are estimated, the inversion for the estimated velocity is performed according to (40). An assessment of inversion quality is made with the same cross-validation method employed to evaluate spatial APS removal, as shown in Fig. 6.

All temporal inversion approaches result in a lower variance of residual velocities for stable areas than the inversion of the velocity performed on the individual interferograms.

The differences in performance between the temporal covariance models appear not to be significant, with both cases considering either the decorrelation or the APS only showing a very similar residual distribution as the OLS inversion. This is quantified in Table II, where the bias and standard deviation for the *APS+Coh*, *Coh*, and *OLS* covariance models are almost identical for all spatial APS correction approaches.

Including the Brownian coherence decay model does not affect the estimation of standard deviation and bias, because these parameters are estimated using cross-validation on a set of PS, which are not affected by temporal decorrelation.

Similarly, including the APS covariance model seems not to reduce significantly the variance of the estimates. This could be explained by the short temporal correlation, as shown in Fig. 5(b): after 500 s, the semivariance attains a value very close to the sill, implying that the APS is not significantly correlated with the close acquisitions. A higher sampling rate— or equivalently shorter acquisition repeat times—is necessary to observe temporal correlation, suggesting the potential for future studies.

In the data set analyzed by this article, including the temporal APS covariance model in the pixelwise inversion does not appreciably change the estimation performance. Therefore, the covariance model could be reduced to the one used for spaceborne InSAR [39], where the APS is assumed uncorrelated with time.

An analysis of the general pattern of the estimated LOS velocity fields can be made considering the plots in Fig. 8.

In Fig. 8(a), the velocity maps were generated directly from uncorrected interferograms, by converting the phases into daily displacement velocities.

These maps appear to capture the spatial patterns of motion known from previous optical observations, where the highest velocities were observed at the glacier's tongue and near the upper and lower icefalls. However, an overestimation of the displacement rates on the areas located outside of the glacier— which should not move during the timespan covered by the acquisitions—is observed. The overestimation is presumably caused by the uncompensated APS.

The overestimation is reduced in Fig. 8(c), showing the standard deviation of the estimates obtained by extrapolating the APS using regression-Kriging and then applying the pixelwise GLS inversion with the *APS+Coherence* covariance model. Note again that there is almost no difference in bias and variance between the OLS and GLS estimates, which is not surprising considering the small temporal correlation observed in the variograms.

Finally, a visualization of the spatial distribution of correction and estimation quality is shown in Fig. 9 in the second and third rows, which display the temporal standard deviation of the velocity estimates for several combinations of APS correction and covariance models used for the GLS inversion.

As seen in the velocity histograms in Fig. 6, there is no difference in the velocity-estimation variance across the solution obtained combining regression-Kriging and an OLS inversion [Fig. 9(f)] and the GLS solution considering the temporal correlation due to the APS and to the decorrelation signal [Fig. 9(i)]. This seems plausible given the short correlation time of the APS, as determined by the means of the temporal variogram in Fig. 5(b).

VI. CONCLUSION

This article presents a study on the estimation and correction of the APS in Ku-band TRI. The APS is among the largest factors affecting the precision of displacement estimates in radar interferometry. While for spaceborne SAR interferometry, a vast literature of approaches for APS modeling and mitigation is available, and only few studies are dedicated to the APS in TRI.

This article addresses several aspects of the modeling and correction of APS for TRI. To do so, it proposes an expansion of the common APS model tailored to TRI. The conventional model—a combination of a stratified atmospheric contribution and of a temporally uncorrelated, spatially correlated stochastic term describing turbulence—is modified by allowing the APS to be correlated with time to account for the short revisit times. To reduce its complexity, the covariance structure of the turbulent component is assumed to be stationary in space and time and separable. Under this assumption, covariance model parameters are fit by performing marginal spatial and temporal variogram analysis on a large set of interferograms acquired at different times.

This framework is the foundation of a method for APS correction based on an interferogram stack, from which a set of PSs unaffected by displacement is determined. The

interferometric phase observations at these PSs—assumed to contain solely an APS contribution—are used to extrapolate the APS to a regular grid covering the interferograms using regression-Kriging, which accounts for both a model of atmospheric stratification and for the spatial correlation of the atmospheric turbulence. Since separable spatiotemporal statistics are assumed, the interpolation is performed using a single covariance function for the entire stack.

By this method, a phase-calibrated stack is obtained, where the residual nuisances, namely, unmodeled APS and decorrelation, are assumed spatially uncorrelated. In this manner, a pixelwise GLS estimator using the temporal covariance model can be applied to the phase-calibrated stack to estimate the displacement rates. The advantage of considering the temporal correlation structure lies in more accurate uncertainty estimates for the displacement parameters.

The proposed approach is tested using a Ku-band radar data set over the Bisgletscher, southwestern Swiss Alps. Regression analysis using a set of PSs located on stable areas shows that stratification models have a poor ability to explain a significant portion of the phase variance caused by the APS, highlighting the importance of statistical description of the turbulent APS.

Variogram analysis suggests that a separable spatiotemporal covariance model is a sufficient approximation to obtain the realistic displacement estimate and that the APS only shows a weak correlation with time. The spatial covariance function derived from this analysis is used for the regression-Kriging APS phase calibration, whose performance is evaluated by estimating the residual velocities at the locations known not to be affected by displacements.

This analysis shows a significant reduction in phase variance after the regression-Kriging-based phase calibration. The same performance analysis is repeated with the output of the time-series inversion applied on calibrated interferograms, obtaining a reduction in the residual phase variance at the cost of a coarser temporal resolution caused by the simplified displacement model. Because of the observed low temporal correlation of the noise in this case study, the use of that correlation structure in the time-series inversion does not improve estimation variance. This could be different in situations of longer correlation times, which would require carefully designed experiments to be observed.

REFERENCES

[1] J. Faillettaz, M. Funk, and C. Vincent, "Avalanching glacier instabilities: Review on processes and early warning perspectives," *Rev. Geophys.*, vol. 53, no. 2, pp. 203–224, Jun. 2015.

[2] A. Pralong and M. Funk, "On the instability of avalanching glaciers," *J. Glaciol.*, vol. 52, no. 176, pp. 31–48, 2006.

[3] H. Röthlisberger and P. Kasser. (1981). *Gletscher und Klima– Glaciers et Climat, Jahrbuch der Schweizerischen Naturforschenden Gesellschaft, Wissenschaftlicher 1978*. [Online]. Available: https://pdfs.semanticscholar.org/b352/2564d738593da09c8261be37933363613f57.pdf

[4] W. Haeberli *et al.*, "The kolka-karmadon rock/ice slide of 20 September 2002: An extraordinary event of historical dimensions in north ossetia, russian caucasus," *J. Glaciol.*, vol. 50, no. 171, pp. 533–546, 2004.

[5] A. Flotron, "Movement studies on a hanging glacier in relation with an ice avalanche," *J. Glaciol.*, vol. 19, no. 81, pp. 671–672, 1977. [Online]. Available: https://www.cambridge.org/core/product/identifier/S0022143000029592/typ%e/journal_article

[6] J. Faillettaz, A. Pralong, M. Funk, and N. Deichmann, "Evidence of log-periodic oscillations and increasing icequake activity during the breaking-off of large ice masses," *J. Glaciol.*, vol. 54, no. 187, pp. 725–737, 2008. [Online]. Available: http://openurl.ingenta.com/content/xref?genre=article&issn=0022-1430%&volume=54&issue=187&spage=725 and http://www.ingentaconnect.com/content/igsoc/jog/2008/00000054/00000187/art00%016

[7] H. Röthlisberger, "Sliding phenomena in a steep section of balmhorn-gletscher, Switzerland," *J. Geophys. Res.*, vol. 92, no. B9, p. 8999, 1987.

[8] P. D. Canassy, J. Faillettaz, F. Walter, and M. Huss, "Seismic activity and surface motion of a steep temperate glacier: A study on trift-gletscher, switzerland," *J. Glaciol.*, vol. 58, no. 209, pp. 513–528, 2012.

[9] G. Luzi *et al.*, "Monitoring of an alpine glacier by means of ground-based SAR interferometry," *IEEE Geosci. Remote Sens. Lett.*, vol. 4, no. 3, pp. 495–499, Jul. 2007. [Online]. Available: http://ieeexplore.ieee.org/document/4271456

[10] A. Kääb, R. Wessels, W. Haeberli, C. Huggel, J. S. Kargel, and S. J. S. Khalsa, "Rapid ASTER imaging facilitates timely assessment of glacier hazards and disasters," *EOS, Trans. Amer. Geophys. Union*, vol. 84, no. 13, p. 117, 2003.

[11] A. Kääb *et al.*, "Remote sensing of glacier- and permafrost-related hazards in high mountains: An overview," *Natural Hazards Earth Syst. Sci.*, vol. 5, no. 4, pp. 527–554, Jul. 2005.

[12] E. Berthier *et al.*, "Surface motion of mountain glaciers derived from satellite optical imagery," *Remote Sens. Environ.*, vol. 95, pp. 14–28, Mar. 2005.

[13] A. Kääb, "Monitoring high-mountain terrain deformation from repeated air- and spaceborne optical data: Examples using digital aerial imagery and ASTER data," *ISPRS J. Photogram. Remote Sens.*, vol. 57, nos. 1–2, pp. 39–52, Nov. 2002.

[14] T. A. Scambos, M. J. Dutkiewicz, J. C. Wilson, and R. A. Bindschadler, "Application of image cross-correlation to the measurement of glacier velocity using satellite image data," *Remote Sens. Environ.*, vol. 42, no. 3, pp. 177–186, Dec. 1992.

[15] R. M. Goldstein, H. Engelhardt, B. Kamb, and R. M. Frolich, "Satellite radar interferometry for monitoring ice sheet motion: Application to an Antarctic ice stream," *Science*, vol. 262, no. 5139, pp. 1525–1530, Dec. 1993.

[16] A. L. Gray, N. Short, K. E. Mattar, and K. C. Jezek, "Velocities and flux of the Filchner ice shelf and its tributaries determined from speckle tracking interferometry," *Can. J. Remote Sens.*, vol. 27, no. 3, pp. 193–206, Jun. 2001.

[17] T. Strozzi, A. Luckman, T. Murray, U. Wegmüller, and C. L. Werner, "Glacier motion estimation using SAR offset-tracking procedures," *IEEE Trans. Geosci. Remote Sens.*, vol. 40, no. 11, pp. 2384–2391, Nov. 2002.

[18] I. Joughin, R. Kwok, and M. Fahnestock, "Estimation of ice-sheet motion using satellite radar interferometry: Method and error analysis with application to humboldt glacier, greenland," *J. Glaciol.*, vol. 42, no. 142, pp. 564–575, 1996. [Online]. Available: https://www.cambridge.org/core/product/identifier/S0022143000003543/typ%e/journal_article

[19] B. T. Rabus and D. R. Fatland, "Comparison of SAR-interferometric and surveyed velocities on a mountain glacier: Black rapids glacier, alaska, U.S.A.," *J. Glaciol.*, vol. 46, no. 152, pp. 119–128, 2000.

[20] R. Michel and E. Rignot, "Flow of glaciar Moreno, Argentina, from repeat-pass shuttle imaging radar images: Comparison of the phase correlation method with radar interferometry," *J. Glaciol.*, vol. 45, no. 149, pp. 93–100, 1999.

[21] K. E. Allstadt, D. E. Shean, A. Campbell, M. Fahnestock, and S. D. Malone, "Observations of seasonal and diurnal glacier velocities at mount rainier, Washington, using terrestrial radar interferometry," *Cryosphere*, vol. 9, no. 6, pp. 2219–2235, Dec. 2015.

[22] D. Voytenko *et al.*, "Multi-year observations of Breiamerkurjökull, a marine-terminating glacier in Southeastern iceland, using terrestrial radar interferometry," *J. Glaciol.*, vol. 61, no. 225, pp. 42–54, 2015.

[23] T. H. Dixon *et al.*, "Emerging technology monitors ice-sea interface at outlet glaciers," *Eos, Trans. Amer. Geophys. Union*, vol. 93, no. 48, pp. 497–498, Nov. 2012.

[24] L. Noferini, D. Mecatti, G. Macaluso, M. Pieraccini, and C. Atzeni, "Monitoring of belvedere glacier using a wide angle GB-SAR inter-ferometer," *J. Appl. Geophys.*, vol. 68, no. 2, pp. 289–293, Jun. 2009.

This article has been accepted for inclusion in a future issue of this journal. Content is final as presented, with the exception of pagination.

22   IEEE TRANSACTIONS ON GEOSCIENCE AND REMOTE SENSING

[25] D. Mecatti *et al.*, "Remote sensing of glacier by ground-based radar interferometry," in *Proc. IEEE Int. Geosci. Remote Sens. Symp.*, Jul. 2007, pp. 4501–4504.

[26] D. Massonnet and K. L. Feigl, "Radar interferometry and its application to changes in the Earth's surface," *Rev. Geophys.*, vol. 36, no. 4, pp. 441–500, Nov. 1998.

[27] M. Bevis, S. Businger, T. A. Herring, C. Rocken, R. A. Anthes, and R. H. Ware, "GPS meteorology: Remote sensing of atmospheric water vapor using the global positioning system," *J. Geophys. Res.*, vol. 97, no. D14, p. 15787, 1992.

[28] R. F. Hanssen, "Atmospheric heterogeneities in ERS tandem SAR interferometry," Delft Univ., Delft, The Netherlands, Tech. Rep., 1998.

[29] R. N. Treuhaft and G. E. Lanyi, "The effect of the dynamic wet tro- posphere on radio interferometric measurements," *Radio Sci.*, vol. 22, no. 2, pp. 251–265, Mar. 1987.

[30] R. F. Hanssen, *Radar Interferometry* (Remote Sensing and Digital Image Processing), vol. 2. Amsterdam, The Netherlands: Springer, 2001. [Online]. Available: http://www.iub.edu/~act/files/publications/ 2004/04-12_LUCCPathways%_Impacts.pdf, http://link.springer.com/ 10.1007/0-306-47633-9, and http://www.nature.com/doifinder/10. 1038/scientificamerican0297-46

[31] J. Jung, D.-J. Kim, and S.-E. Park, "Correction of atmospheric phase screen in time series InSAR using WRF model for monitoring vol- canic activities," *IEEE Trans. Geosci. Remote Sens.*, vol. 52, no. 5, pp. 2678–2689, May 2014.

[32] T. R. Emardson, M. Simons, and F. H. Webb, "Neutral atmospheric delay in interferometric synthetic aperture radar applications: Statistical description and mitigation," *J. Geophys. Res., Solid Earth*, vol. 108, no. B5, p. 2231, May 2003.

[33] F. Onn and H. A. Zebker, "Correction for interferometric synthetic aperture radar atmospheric phase artifacts using time series of zenith wet delay observations from a GPS network," *J. Geophys. Res.*, vol. 111, no. B9, pp. 1–16, 2006.

[34] S. Williams, Y. Bock, and P. Fang, "Integrated satellite interferometry: Tropospheric noise, GPS estimates and implications for interferometric synthetic aperture radar products," *J. Geophys. Res., Solid Earth*, vol. 103, no. B11, pp. 27051–27067, Nov. 1998.

[35] P. Basili, S. Bonafoni, V. Mattioli, P. Ciotti, and N. Pierdicca, "Mapping the atmospheric water vapor by integrating microwave radiometer and GPS measurements," *IEEE Trans. Geosci. Remote Sens.*, vol. 42, no. 8, pp. 1657–1665, Aug. 2004.

[36] Z. Li, J. P. Muller, P. Cross, P. Albert, J. Fischer, and R. Ben- nartz, "Assessment of the potential of MERIS near-infrared water vapour products to correct ASAR interferometric measurements," *Int. J. Remote Sens.*, vol. 27, no. 2, pp. 349–365, Jan. 2006.

[37] Z. W. Li *et al.*, "Correcting atmospheric effects on InSAR with MERIS water vapour data and elevation-dependent interpolation model," *Geo- phys. J. Int.*, vol. 189, no. 2, pp. 898–910, May 2012.

[38] Z. Li, E. J. Fielding, P. Cross, and R. Preusker, "Advanced InSAR atmospheric correction: MERIS/MODIS combination and stacked water vapour models," *Int. J. Remote Sens.*, vol. 30, no. 13, pp. 3343–3363, Jul. 2009.

[39] P. S. Agram and M. Simons, "A noise model for InSAR time series," *J. Geophys. Res., Solid Earth*, vol. 120, no. 4, pp. 2752–2771, Apr. 2015.

[40] R. Jolivet *et al.*, "Improving InSAR geodesy using global atmospheric models," *J. Geophys. Res., Solid Earth*, vol. 119, no. 3, pp. 2324–2341, Mar. 2014.

[41] L. Pipia, X. Fabregas, A. Aguasca, and C. Lopez-Martinez, "Atmospheric artifact compensation in ground-based DInSAR appli- cations," *IEEE Geosci. Remote Sens. Lett.*, vol. 5, no. 1, pp. 88–92, Jan. 2008. [Online]. Available: http://ieeexplore.ieee.org/document/ 4383036/

[42] L. Noferini *et al.*, "Permanent scatterers analysis for atmospheric correction in ground-based SAR interferometry," *IEEE Trans. Geosci. Remote Sens.*, vol. 43, no. 7, pp. 1459–1471, Jul. 2005.

[43] G. Luzi *et al.*, "Ground-based radar interferometry for landslides monitoring: Atmospheric and instrumental decorrelation sources on experimental data," *IEEE Trans. Geosci. Remote Sens.*, vol. 42, no. 11, pp. 2454–2466, Nov. 2004.

[44] A. M. Guarnieri, L. Iannini, and D. Giudici, "On the exploitation of meteo information for atmospheric phase screen compensation in GB-SAR interferometry," in *Proc. ESA Living Planet Symp.*, 2010. [Online]. Available: https://ui.adsabs.harvard.edu/abs/2010ESASP. 686E.275M/abstract

[45] R. Iglesias *et al.*, "Atmospheric phase screen compensation in ground-based SAR with a multiple-regression model over mountain- ous regions," *IEEE Trans. Geosci. Remote Sens.*, vol. 52, no. 5, pp. 2436–2449, May 2014.

[46] R. Iglesias *et al.*, "Ground-based polarimetric SAR interferometry for the monitoring of terrain displacement phenomena—Part I: Theoretical description," *IEEE J. Sel. Topics Appl. Earth Observ. Remote Sens.*, to be published. [Online]. Available: http://ieeexplore.ieee.org/lpdocs/ epic03/wrapper.htm?arnumber=6981929 and http://ieeexplore.ieee.org/ lpdocs/epic03/wrapper.htm?arnumber=6982213

[47] N. Dematteis, G. Luzi, D. Giordan, F. Zucca, and P. Allasia, "Monitor- ing alpine glacier surface deformations with GB-SAR," *Remote Sens. Lett.*, vol. 8, no. 10, pp. 947–956, Oct. 2017.

[48] P. W. Webley, G. Wadge, and I. N. James, "Determining radio wave delay by non-hydrostatic atmospheric modelling of water vapour over mountains," *Phys. Chem. Earth, Parts A/B/C*, vol. 29, nos. 2–3, pp. 139–148, Jan. 2004.

[49] J. P. M. Boncori and J. J. Mohr, "Statistical description of tropospheric delay for InSAR: Overview and a new model," in *Proc. IEEE Int. Geosci. Remote Sens. Symp.*, Jul. 2007, pp. 4483–4486.

[50] A. Ferretti, C. Prati, and F. Rocca, "Permanent scatterers in SAR interferometry," *IEEE Trans. Geosci. Remote Sens.*, vol. 39, no. 1, pp. 8–20, Jan. 2001.

[51] C. Werner, U. Wegmüller, T. Strozzi, and A. Wiesmann, "Interferomet- ric point target analysis for deformation mapping," in *Proc. IEEE Int. Geosci. Remote Sens. Symp.*, vol. 7, Jul. 2003, pp. 4362–4364.

[52] M. Crosetto, O. Monserrat, M. Cuevas-González, N. Devanthéry, and B. Crippa, "Persistent scatterer interferometry: A review," *ISPRS J. Photogram. Remote Sens.*, vol. 115, pp. 78–89, May 2016.

[53] D. G. Krige, "A statistical approach to some mine valuation and allied problems on the Witwatersrand," Dept. Sci. Eng., Univ. Witwatersrand, Johannesburg, South Africa, 1951.

[54] A. Ferretti, C. Prati, and F. Rocca, "Nonlinear subsidence rate esti- mation using permanent scatterers in differential SAR interferometry," *IEEE Trans. Geosci. Remote Sens.*, vol. 38, no. 5, pp. 2202–2212, Sep. 2000.

[55] A. Hooper, H. Zebker, P. Segall, and B. Kampes, "A new method for measuring deformation on volcanoes and other natural terrains using InSAR persistent scatterers," *Geophys. Res. Lett.*, vol. 31, no. 23, Dec. 2004.

[56] L. Iannini and A. Monti Guarnieri, "Atmospheric phase screen in ground-based radar: Statistics and compensation," *IEEE Geosci. Remote Sens. Lett.*, vol. 8, no. 3, pp. 537–541, May 2011.

[57] D. Massonnet and T. Rabaute, "Radar interferometry: Limits and poten- tial," *IEEE Trans. Geosci. Remote Sens.*, vol. 31, no. 2, pp. 455–464, Mar. 1993.

[58] P. Rosen *et al.*, "Synthetic aperture radar interferometry," *Proc. IEEE*, vol. 88, no. 3, pp. 333–382, Mar. 2000. [Online]. Avail- able: http://ieeexplore.ieee.org/lpdocs/epic03/wrapper.htm?arnumber= 838084

[59] P. Berardino, G. Fornaro, R. Lanari, and E. Sansosti, "A new algo- rithm for surface deformation monitoring based on small baseline differential SAR interferograms," *IEEE Trans. Geosci. Remote Sens.*, vol. 40, no. 11, pp. 2375–2383, Nov. 2002. [Online]. Available: http://ieeexplore.ieee.org/document/1166596/

[60] R. Lanari *et al.*, "An overview of the small baseline subset algorithm: A DInSAR technique for surface deformation analysis," *Pure Appl. Geophys.*, vol. 164, pp. 637–661, Apr. 2007. [Online]. Available: http://www.springerlink.com/index/10.1007/978-3-7643- 8417-3_2

[61] R. Snieder and J. Trampert, "Inverse problems in geophysics," in *Wavefield Inversion*. Vienna, Austria: Springer, 1999, pp. 119–190.

[62] A. Tarantola and B. Valette, "Inverse problems—quest for information," *J. Geophys.*, vol. 50, no. 1, pp. 159–170, 1982.

[63] B. M. Kampes, *Radar Interferometry*. Amsterdam, The Netherlands: Springer, 2006. [Online]. Available: http://www.iub.edu/~act/files/ publications/2004/04-12_LUCCPathways%_Impacts.pdf http://link.springer.com/10.1007/978-1-4020-4723-7

[64] H. A. Zebker and J. Villasenor, "Decorrelation in interferomet- ric radar echoes," *IEEE Trans. Geosci. Remote Sens.*, vol. 30, no. 5, pp. 950–959, Sep. 1992. [Online]. Available: http://ieeexplore. ieee.org/lpdocs/epic03/wrapper.htm?arnumber=175330

[65] R. Touzi, A. Lopes, J. Bruniquel, and P. W. Vachon, "Coherence estimation for SAR imagery," *IEEE Trans. Geosci. Remote Sens.*, vol. 37, no. 1, pp. 135–149, Jan. 1999.

[66] E. Rodriguez and J. M. Martin, "Theory and design of interferometric synthetic aperture radars," *IEE Proc. F Radar Signal Process.*, vol. 139, no. 2, p. 147, 1992.

[67] F. Rocca, "Modeling interferogram stacks," *IEEE Trans. Geosci. Remote Sens.*, vol. 45, no. 10, pp. 3289–3299, Oct. 2007. [Online]. Available: http://ieeexplore.ieee.org/document/4305374/

[68] T. Gneiting, M. Genton, and P. Guttorp, "Geostatistical space-time models, stationarity, separability, and full symmetry," in *Statistical Methods for Spatio-Temporal Systems*. London, U.K.: Chapman & Hall, 2006, pp. 151–175.

[69] V. K. Gupta and E. Waymire, "On Taylor's hypothesis and dissipation in rainfall," *J. Geophys. Res., Atmos.*, vol. 92, pp. 9657–9660, Aug. 1987.

[70] R. F. Hanssen, "High-resolution water vapor mapping from interferometric radar measurements," *Science*, vol. 283, no. 5406, pp. 1297–1299, Feb. 1999. [Online]. Available: http://www.ncbi.nlm.nih.gov/pubmed/10037594

[71] M. G. Genton, "Separable approximations of space-time covariance matrices," *Environmetrics*, vol. 18, no. 7, pp. 681–695, Nov. 2007.

[72] R. S. Bivand, E. J. Pebesma, and V. Gómez-Rubio, *Applied Spatial Data Analysis With R (Use R)*, vol. 1. New York, NY, USA: Springer, 2008, p. 378.

[73] W. H. Greene, "The generalized regression model: Heteroscedasticity," in *Econometric Analysis*, 7th ed. London, U.K.: Pearson, 2012, ch. 9.

[74] H. Wackernagel, *Multivariate Geostatistics*. Berlin, Germany: de Gruyter, 2003.

[75] J. Butt, A. Wieser, and S. Conzett, "Intrinsic random functions for mitigation of atmospheric effects in terrestrial radar interferometry," *J. Appl. Geodesy*, vol. 11, no. 2, pp. 89–98, Jan. 2017.

[76] G. Matheron, "The intrinsic random functions and their applications," *Adv. Appl. Probab.*, vol. 5, no. 03, pp. 439–468, Dec. 1973. [Online]. Available: http://www.jstor.org/stable/1425829 http://cg.ensmp.fr/bibliotheque/public/MATHERON_Publication_00180.pdf%%5Cnhttp://www.jstor.org/stable/1425829?origin=crossref

[77] K. G. van den Boogaart and A. Brenning, "Why universal Kriging is better than IRFk-Kriging: Estimation of variograms in the presence of trend," Tech. Rep., 2001. [Online]. Available: https://pdfs.semanticscholar.org/b352/2564d738593da09c8261be37933363613f57.pdf

[78] R. Christensen, "The equivalence of predictions from universal kriging and intrinsic random-function kriging," *Math. Geol.*, vol. 22, no. 6, pp. 655–664, Aug. 1990.

[79] N. Blaunstein and C. Christodoulou, *Radio Propagation and Adaptive Antennas for Wireless Communication Links (Wiley Series in Microwave and Optical Engineering)*, vol. 8. Hoboken, NJ, USA: Wiley, Nov. 2006.

[80] H. Akaike, "A new look at the statistical model identification," *IEEE Trans. Autom. Control*, vol. AC-19, no. 6, pp. 716–723, Dec. 1974.

[81] H. A. Zebker, P. A. Rosen, and S. Hensley, "Atmospheric effects in interferometric synthetic aperture radar surface deformation and topographic maps," *J. Geophys. Res., Solid Earth*, vol. 102, no. B4, pp. 7547–7563, Apr. 1997.

[82] P. Legendre and L. Legendre, "Spatial analysis," in *Numerical Ecology*, 2nd ed. Amsterdam, The Netherlands: Elsevier, 1998, p. 853.

[83] N. Bliznyuk, R. J. Carroll, M. G. Genton, and Y. Wang, "Variogram estimation in the presence of trend," *Statist. Interface*, vol. 5, no. 2, pp. 159–168, 2012. [Online]. Available: http://www.ncbi.nlm.nih.gov/pubmed/PMC3378336, http://www.ncbi.nlm.nih.gov/pubmed/378336, and http://www.intlpress.com/site/pub/pages/journals/items/sii/content/vols/0005%/0002/a002/

[84] R. Caduff, A. Kos, F. Schlunegger, B. W. McArdell, and A. Wiesmann, "Terrestrial radar interferometric measurement of hillslope deformation and atmospheric disturbances in the illgraben debris-flow catchment, Switzerland," *IEEE Geosci. Remote Sens. Lett.*, vol. 11, no. 2, pp. 434–438, Feb. 2014.

[85] L. Kristensen, C. Rivolta, J. Dehls, and L. H. Blikra, "GB-InSAR measurement at the Åknes rockslide, Norway," in *Proc. Int. Conf. Vajont*, Padua, Italy, Oct. 2013.

[86] S. Tebaldini and A. Monti, "Methods and performances for multi-pass SAR interferometry," in *Geoscience and Remote Sensing New Achievements*. Rijeka, Croatia: InTech, Feb. 2010, pp. 329–357. [Online]. Available: http://cdn.intechopen.com/pdfs/10403/InTech-Methods_and_performan%ces_for_multi_pass_sar_interferometry.pdf

[87] R. Caduff, F. Schlunegger, A. Kos, and A. Wiesmann, "A review of terrestrial radar interferometry for measuring surface change in the geosciences," *Earth Surf. Processes Landforms*, vol. 40, no. 2, pp. 208–228, Feb. 2015.

[88] P. Riesen, T. Strozzi, A. Bauder, A. Wiesmann, and M. Funk, "Short-term surface ice motion variations measured with a ground-based portable real aperture radar interferometer," *J. Glaciol.*, vol. 57, no. 201, pp. 53–60, 2011.

[89] J. Biggs, T. Wright, Z. Lu, and B. Parsons, "Multi-interferogram method for measuring interseismic deformation: Denali fault, alaska," *Geophys. J. Int.*, vol. 170, no. 3, pp. 1165–1179, Sep. 2007.

[90] S. Samiei-Esfahany, J. E. Martins, F. van Leijen, and R. F. Hanssen, "Phase estimation for distributed scatterers in InSAR stacks using integer least squares estimation," *IEEE Trans. Geosci. Remote Sens.*, vol. 54, no. 10, pp. 5671–5687, Oct. 2016.

[91] T. Strozzi, U. Wegmüller, C. Werner, and A. Wiesmann, "Measurement of slow uniform surface displacement with mm/year accuracy," in *Proc. IEEE Int. Geosci. Remote Sens. Symp.*, Jul. 2000, pp. 2239–2241.

[92] S. Baffelli, O. Frey, and I. Hajnsek, "System characterization and polarimetric calibration of the Ku-band advanced polarimetric interferometer," in *Proc. Eur. Conf. Synth. Aperture Radar*, 2016, pp. 2–5.

[93] S. Baffelli, O. Frey, C. Werner, and I. Hajnsek, "Polarimetric calibration of the Ku-band advanced polarimetric radar interferometer," *IEEE Trans. Geosci. Remote Sens.*, vol. 56, no. 4, pp. 2295–2311, Apr. 2018. [Online]. Available: http://ieeexplore.ieee.org/document/8226855/

[94] C. L. Werner, A. Wiesmann, T. Strozzi, A. Kos, R. Caduff, and U. Wegmüller, "The GPRI multi-mode differential interferometric radar for ground-based observations," in *Proc. Eur. Conf. Synth. Aperture Radar*, 2012, pp. 304–307. [Online]. Available: http://ieeexplore.ieee.org/stamp/stamp.jsp?arnumber=06217065

[95] A. G. Stove, "Linear FMCW radar techniques," *IEE Proc. F Radar Signal Process.*, vol. 139, no. 5, p. 343, 1992.

[96] J. Beutel, B. Buchli, F. Ferrari, M. Keller, M. Zimmerling, and L. Thiele, "X-SENSE: Sensing in extreme environments," in *Proc. Design, Autom. Test Eur.*, Mar. 2011, pp. 1–6. [Online]. Available: http://ieeexplore.ieee.org/lpdocs/epic03/wrapper.htm?arnumber=5763236 and http://ieeexplore.ieee.org/search/srchabstract.jsp?tp=&arnumber=5763236%&queryText%3D%28sensing+in+extreme+environments%29%26openedRefine%ments%3D*%26matchBoolean%3Dtrue%26rowsPerPage%3D3

[97] *Federal Office For Topography (Swisstopo)*. Accessed: Dec. 2018. [Online]. Available: https://www.geocat.ch/geonetwork/srv/ger/md.viewer#/full_view/4c8c7c58%-61c7-4a61-8e7a-6ffb95d183df/tab/complete

[98] U. Wegmüller, O. Frey, and C. L. Werner, "Point density reduction in persistent scatterer interferometry," in *Proc. Eur. Conf. Synth. Aperture Radar*, 2012, pp. 673–676. [Online]. Available: http://ieeexplore.ieee.org/document/6217159/

[99] P. Di Tommaso, M. Chatzou, E. W. Floden, P. P. Barja, E. Palumbo, and C. Notredame, "Nextflow enables reproducible computational workflows," *Nature Biotechnol.*, vol. 35, no. 4, pp. 316–319, Apr. 2017.

[100] Federal Office For Topography (Swisstopo). *Geographical Names swissNAMES3D*. [Online]. Available: https://www.geocat.ch/geonetwork/srv/ita/catalog.search#/metadata/ab24%e5cc-7f53-451a-820a-f113fa545943

[101] D. Myers, "Estimating and modeling space-time variograms," in *Proc. Joint Meeting 6th Int. Symp. Spatial Accuracy Assessment Natural Resour. Environ. Sci., 15th Annu. Conf. Int. Environmetrics Soc.*, 2004.

[102] E. Gringarten and C. V. Deutsch, "Teacher's aide variogram interpretation and modeling," *Math. Geol.*, vol. 33, no. 4, pp. 507–534, 2001.

[103] A. Refice, A. Belmonte, F. Bovenga, and G. Pasquariello, "On the use of anisotropic covariance models in estimating atmospheric DInSAR contributions," *IEEE Geosci. Remote Sens. Lett.*, vol. 8, no. 2, pp. 341–345, Mar. 2011.

[104] S. Knospe and S. Jonsson, "Covariance estimation for dInSAR surface deformation measurements in the presence of anisotropic atmospheric noise," *IEEE Trans. Geosci. Remote Sens.*, vol. 48, no. 4, pp. 2057–2065, Apr. 2010.

Simone Baffelli (Student Member, IEEE) received the B.Sc. and M.Sc. degrees in electrical engineering from the Swiss Federal Institute of Technology (ETH), Zürich, Switzerland, in 2011 and 2013, respectively, and the Dr.Sc. (Ph.D.) degrees from the Chair of Earth Observation and Remote Sensing, Swiss Federal Institute of Technology, in 2019.

His research interests include the use of ground-based radar systems for the mapping of surface displacement, the analysis and correction of atmospheric phase screen in terrestrial differential interferometry, and the processing, calibration, and applications of polarimetric terrestrial radar data.

Othmar Frey (Senior Member, IEEE) received the M.Sc. degree (Hons.) in geomatic engineering from ETH Zürich, Zürich, Switzerland, in 2002, and the Ph.D. (Dr.sc. nat.) degree (Hons.) in radar remote sensing from the University of Zurich, Zürich, in 2010.

He is a tenured Senior Researcher and Lecturer with ETH Zürich, and also a Senior Scientist with GAMMA Remote Sensing AG, Gümligen, Switzerland. He has been working in this joint academic/industry setting since 2011. From 2002 to 2010, he was a Research Associate with the Remote Sensing Laboratory, University of Zurich. He has been active in various national and international research projects, as a PI and Project Manager, as well as a Co-Investigator. At GAMMA, he has also been active in the development of the Gamma Software and in technical consulting related to SAR imaging and interferometric applications. He has been a member of the SAOCOM-CS Science Expert Group, European Space Agency. His research encompasses 2-D and 3-D (tomographic) synthetic aperture radar (SAR) focusing techniques and interferometric techniques for applications, such as 3-D forest mapping, ground deformation monitoring (persistent scatterer interferometry/differential tomography), and profiling the structure of snowpacks, using spaceborne, airborne, and terrestrial radar sensors.

Dr. Frey received the Distinction Award and Prize from the Faculty of Science, University of Zurich, for his Ph.D. thesis, in 2010, and he received the ETH Medal for an outstanding M.Sc. thesis in 2002. He was a recipient of the Third Place Student Paper Award at the 2010 EUSAR Conference in Aachen, Germany, and he was a co-recipient of the Best Paper Award at the ISPRS Workshop Laserscanning and Silvilaser 2007 in Helsinki, Finland. Since 2015, he has been the Chair of the Swiss Chapter of the IEEE Geoscience and Remote Sensing Society.

Irena Hajnsek (Fellow, IEEE) received the Diploma degree (Hons.) from the Free University of Berlin, Berlin, Germany, in 1996, and the Doctor degree (Hons.) from Friedrich Schiller University Jena, Jena, Germany, in 2001.

Since November 2009, she has been a Professor of Earth Observation with the Institute of Environmental Engineering, Swiss Federal Institute of Technology (ETH) Zürich, Zürich, Switzerland, and, at the same time, the Head of the Polarimetric SAR Interferometry Group, Microwaves and Radar Institute (HR), German Aerospace Center (DLR), Wessling, Germany. From 1996 to 1999, she was with DLR-HR. From 1999 to 2000, she was with the Institut d'Electronique et de Telecommunications de Rennes, University of Rennes 1, Rennes, France, for ten months, in the frame of the EC-TMR Radar Polarimetry Network. In 2005, she was a Guest Scientist with the University of Adelaide, Adelaide, Australia, for six weeks. She is the Science Coordinator of German satellite mission TanDEM-X. Her main research interests are in electromagnetic propagation and scattering theory, radar polarimetry, SAR and interferometric SAR data processing techniques, and environmental parameter modeling and estimation.

Dr. Hajnsek was a member of the ESA Mission Advisory Group of the Seventh Explorer Mission CoReH2O from 2009 to 2013. Since 2013, she has been a member of the IEEE Geoscience and Remote Sensing Society Administrative Committee. She was a Technical Program Co-Chair of the 2012 IEEE International Geoscience and Remote Sensing Symposium in Munich.